Inherent length scales of periodic mesoscale density structures in the solar wind over two solar cycles

L. Kepko[1], N. M. Viall[1], K. Wolfinger[2]

[1]NASA Goddard Space Flight Center, Greenbelt, MD, USA. [2]University of Colorado Boulder, Boulder, Colorado, USA.

Key Points:

- 25 years of Wind solar wind data are analyzed for periodic mesoscale structures in the proton density
- Periodic density structures recur with particular length scales, suggesting solar formation
- The observed length scales are solar cycle dependent

Corresponding author: L Kepko, `larry.kepko@nasa.gov`

Abstract

It is now well-established through multiple event and statistical studies that the solar wind at 1 AU contains contains periodic, mesoscale ($L \sim 100 - 1000$ Mm) structures in the proton density. Composition variations observed at 1 AU within periodic density structures and remote sensing observations of similar structures in the young solar wind indicate that at least some of these periodic structures originate in the solar atmosphere as a part of solar wind formation. Viall et al. (2008) analyzed 11 years of data from the Wind spacecraft near L1 and demonstrated a recurrence to the length scales of periodic structures in the solar wind proton density observed, and a potential solar cycle dependence. In the time since that study, Wind has collected 14 additional years of solar wind data, allowing a more thorough examination of the dependence of these structures as a function of solar cycle. In addition, the Wind plasma data have been reprocessed in the interim, and new methods for spectral background approximation have been developed, allowing a reevaluation of the precision and accuracy of the initial study. In this study, we analyze 25 years of Wind data collected near L1, and produce occurrence distributions of statistically significant periodic length scales in proton density. The results confirm the Viall et al. (2008) study and significantly extend those results to show a solar cycle dependence of the length scales, and a possible relation to solar "termination" events.

Plain Language Summary

The plasma and magnetic field in the solar atmosphere flows away from the Sun, filling interplanetary space. This plasma is called the solar wind, and it constantly bombards all of the planets in the solar system. The solar wind is comprised of mesoscale structures - larger than scales where particle dynamics are important, but smaller than global scales - of increased density, and therefore pressure. They are of order the size of Earth's magnetosphere, and often quasi-periodic. These periodic density structures are an important driver of dynamics in Earth's space environment. In this study, we examine the statistics of the size scales of these structures using 25 years, or approximately two solar cycles, of Wind spacecraft solar wind data. We confirm earlier work showing a persistence of particular length scales to the periodicities, and find that the periodicities are a function of solar cycle. In addition to their driving of magnetospheric dynamics, periodic density structures are a tracer of solar wind formation. Their lengths scales and evolution are an important constraint of solar wind formation.

1 Introduction

The solar wind often contains intervals of mesoscale ($L \sim 100-1000$ Mm), quasi-periodic proton density enhancements, termed periodic density structures (PDSs). They were initially discovered through event studies that showed a direct correspondence between magnetospheric pulsations in the mHz range and a one-to-one correlation with discrete frequencies in the solar wind density observed in the upstream solar wind (Kepko et al., 2002; Kepko & Spence, 2003). Numerous event studies have observed similar direct links between the periodicities in solar wind density and periodicities in radar (Stephenson & Walker, 2002; Fenrich & Waters, 2008), ionospheric (Dyrud et al., 2008), and ground magnetometer (Villante et al., 2007; Villante & Tiberi, 2016) observations.

At frequencies $<\sim$ 4 mHz the magnetosphere is generally incapable of supporting standing oscillations, such as via cavity mode or fieldline resonances (e.g., Hartinger et al. (2013)). Meanwhile, PDSs have been observed to directly drive magnetospheric pulsations from ~ 4 mHz down to ~ 0.2 mHz. Hence, there is a general split between directly driven oscillations at $f < 4$ mHz, and internally supported oscillations at around $f > 4$ mHz. This divide straddles the traditional Pc5 range of 1.7-6.7 mHz. We further note that solar wind driven pulsations span the Pc5 range but extend to lower frequencies, into the $f < 1.7$ mHz ($T > 600$ s) Pc6 range (Saito, 1978). Pc6 oscillations are rarely included in magnetospheric ULF waves studies, yet these lower frequency solar wind driven oscillations may have important consequences for magnetospheric dynamics (Kepko & Viall, 2019).

While there have been many statistical studies of magnetospheric pulsations in the few mHz range (Mathie et al., 1999; Francia et al., 2005; Takahashi & Ukhorskiy, 2007), to date only two studies have examined the statistical occurrence rate of the solar wind periodic density structures that drive them. Viall, Kepko, and Spence (2009) identified statistically significant frequencies observed in 11 years of Wind proton density data near L1 and 10 years of dayside GOES magnetospheric B_z data. They showed that both the solar wind and dayside magnetosphere contained recurrent, similar sets of observed frequencies. The apparent frequency of a periodic density structures as it flows past Earth and an in situ spacecraft is related to the radial length scale of the structure as $f_{pds} = V_{sw}/L_{pds}$. Viall et al. (2008) used the same solar wind data to demonstrate that L_{pds} are on the order of the dayside magnetosphere and larger. They therefore quasi-statically drive magnetospheric pulsations at a frequency f_{pds}. At the typically observed length scales of $\sim$ 80 to several 100 Mm, this equates to oscillations of a few mHz for nominal solar wind conditions, which are observed as Pc5-6 pulsations in Earth's magnetosphere.

Since the initial papers describing the existence of periodic density structures in the solar wind, there have been several attempts to identify their source. A key measurement are the occurrence distributions of statistically significant frequencies and length scales measured by Viall et al. (2008) and Viall, Kepko, and Spence (2009). These distributions of statistically significant spectral peaks in time series of solar wind density consists of 3 sources: in situ generated structures (e.g., via turbulence); 'false positives' at a rate determined by the chosen confidence thresholds and appropriateness of the background spectral fit; and periodic density structures injected through the process of solar wind formation. The first two of these sources would generate a smoothly varying distribution of observed periodicities, while the third could produce localized occurrence distribution peaks. While it is possible within any segment of solar wind to generate a single occurrence of a PDS by turbulent processes during transit from the Sun to L1, such turbulence-driven generation of structures would show a smooth occurrence distribution of found length scales and frequencies, rather than the recurrent sets of enhancements found by Viall et al. (2008) and Viall, Kepko, and Spence (2009). Although it is theoretically possible that there exists an MHD instability that could generate periodic structures in transit to 1 AU, for example a slow mode wave (Hollweg et al., 2014), to date there has been no published observations of such instabilities on mesoscales. Furthermore, Viall, Spence, and Kasper (2009) found a lower occurrence rate of recurrent solar wind periodicities analyzing frequencies than Viall et al. (2008) did analyzing length scales. This suggests advecting structures, rather than locally generated oscillations or waves at particular frequencies.

Multiple lines of evidence suggest that periodic solar wind density structures are tracers of solar wind formation. In situ observations show composition, magnetic field, and electron strahl changes that indicate magnetic reconnection effects that could only have occurred during solar wind release and acceleration (Viall, Spence, & Kasper, 2009; Kepko et al., 2016; Matteo et al., 2019). Matteo et al. (2019), using Helios data, found anisotropic temperature changes within PDSs that are not observed near L1, consistent with solar formation followed by temperature isotropization while in transit. Remote imaging studies using the Solar Terrestrial Relations Observatory (STEREO)/Sun Earth Connection Coronal and Heliospheric Investigation (SECCHI) white light instruments have identified periodic density structures in the solar corona as close as 2.5 solar radii, observed as they accelerate with the surrounding solar wind (Viall et al., 2010; Viall & Vourlidas, 2015; DeForest et al., 2016, 2018). In short, it is now clear that the solar wind is often formed of quasi-periodic mesoscale plasma density structures released as a part of solar wind formation.

Three factors motivate this investigation. First, while previous studies used only 11 years of data, 25 years of Wind solar wind data are now available, which allows an examination of evolution of the recurrent length scales as a function of two complete solar cycles. Second, the Wind SWE data that the Viall et al. (2008) and Viall, Kepko, and Spence (2009) statistical studies analyzed has recently been reprocessed, providing an opportunity to test the accuracy and precision of those previous results. Third, recent progress on techniques used to identify statistically significant spectral peaks has shown that there are limitations to using the AR(1) background assumption, and suggests a different background assumption may be more appropriate (Vaughan et al., 2011).

2 Methods

2.1 Data processing and quality checks

We follow the general process of data preparation and spectral analysis as the Viall et al. (2008) study. We used the proton number density and proton velocity measured by the Solar Wind Experiment (SWE) onboard the Wind spacecraft (Ogilvie et al., 1995) to examine the characteristics of mesoscale periodic density structures observed over the full lifetime of Wind to this point, from 1995-2019. In the time since the Viall et al. (2008) study, Wind SWE data have been reprocessed, leading to more accurate measurements of the proton number density and velocity (Kasper et al., 2006). The primary impact of that reprocessing on this study is that the velocity increased on average by a few percent, which increases the length-scales by a few percent.

For continuity with and comparison to the Viall et al. (2008) study, we follow the same processing steps prior to the spectral analysis. We first converted the time series of solar wind proton density, $n(t)$, to a length series, $L(t)$, by multiplying each time step by the radial velocity, $v_x(t)$. Then we separated the length series into overlapping segments $L = 9072$ Mm in length, shifting by 252 Mm each segment, and then separated segments into two categories, "fast" ($\overline{v_x} \geq 550$ km/s) or "slow" ($\overline{v_x} < 550$ km/s), based on the average proton velocity for each segment. Since the conversion of the time series to a length series produces an irregularly sampled series that is not compatible with Fourier analysis, we then resampled to common length steps of $\Delta L_s = 35.4$ Mm for slow, and $\Delta L_f = 56.7$ Mm for fast. For slow wind, 9072 Mm is approximately 6 hours of data at the median slow solar wind speed, and the 35.4 Mm ΔL is approximately equivalent to the SWE instrument sampling rate (typically 90-100 seconds) converted to length. Similarly, for the fast wind 9072 Mm is approximately 4 hours, and 56.7 Mm is the equivalent sampling rate multiplied by the median fast speed. Note that the categorization of fast and slow data segments is not an attempt at a physics-based classification of solar wind type, for which speed is not the best measure (Zurbuchen et al., 2002; Roberts et al., 2020; Borovsky, 2012). Rather, these two categories are the result of the effective sampling rate of the data segment.

Figure 1 shows both a slow (panels a-c) and fast (panels d-f) segment of solar wind data comparing the original (blue) and reprocessed (red) SWE data as a time series, and both datasets converted into a length series (panels c and f). These segments are typical of other intervals in that they exhibit the very slight increase of a few percent in velocity in the reprocessed data. The reprocessed data also show differences in higher frequency variations, particularly for the fast wind (see Figure 1d).

For each data segment, we imposed data quality requirements to minimize spurious spectral signals, and do not analyze segments that failed the data quality check. We required that the Wind spacecraft be located at least 50 Earth radii (R_E) upstream of Earth, to exclude any solar wind collected within or near Earth's magnetosphere, or that could be contaminated with foreshock activity. This reduced the number of segments during the early part of the Wind mission, when it occasionally enters Earth's magnetosphere. We remove single point data spikes and interpolated over them. We excluded any segment that contained more than 10% flagged or missing data over the entire segment, or 3% consecutive flagged or missing data. Finally, we excluded segments that contained discontinuous jumps (e.g., shocks) in the number density, since this would introduce "ringing" in the spectra. To determine a discontinuous jump, we subtracted a third order polynomial fit to the data segment, and discarded segments that contained changes in 5-point running averages that exceeded 3.7 standard deviations of the detrended median. The

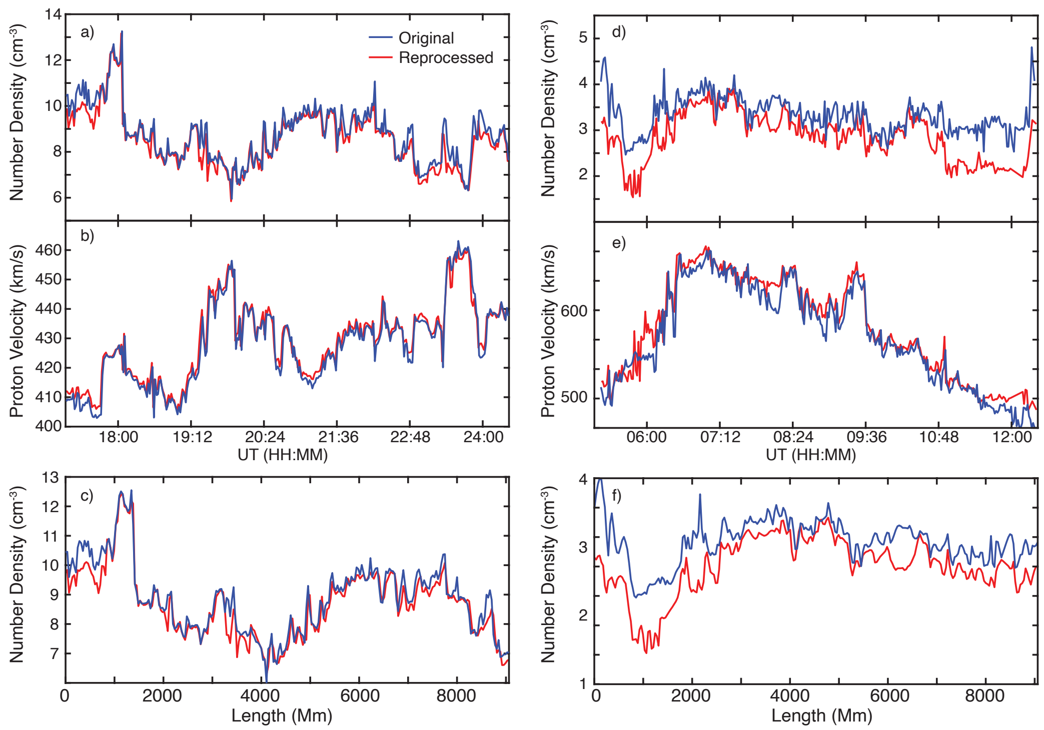

Figure 1. Comparison of the original (blue) and reprocessed (red) solar wind data from Wind SWE for a representative segment, for both slow (left) and fast (right). Reprocessed data show slightly lower density (a and d), slightly higher velocity (b and e), and lower amplitude high frequency variations compared to the original data.

fraction of segments that passed these quality control checks is shown in Figure 2. There is a slight decrease in the number of segments that passed these checks using the reprocessed SWE data for the slow wind compared to the original data used by Viall et al. (2008).

2.2 Spectral analysis and peak detection

We perform spectral analysis on each segment that passed the quality checks. We identify statistically significant spectral speaks using an amplitude test and a harmonic F-test. For the amplitude test, we calculate the spectra, estimate the background fit, then identifying statistically significant peaks above this background. We use the segments in Figure 1c and 1f to demonstrate the process, and present the results in Figure 3. Estimation of the spectra relies on the multitaper method (MTM), in which multiple, orthogonal Slepian tapers are convolved with the data segment to provide multiple, inde-

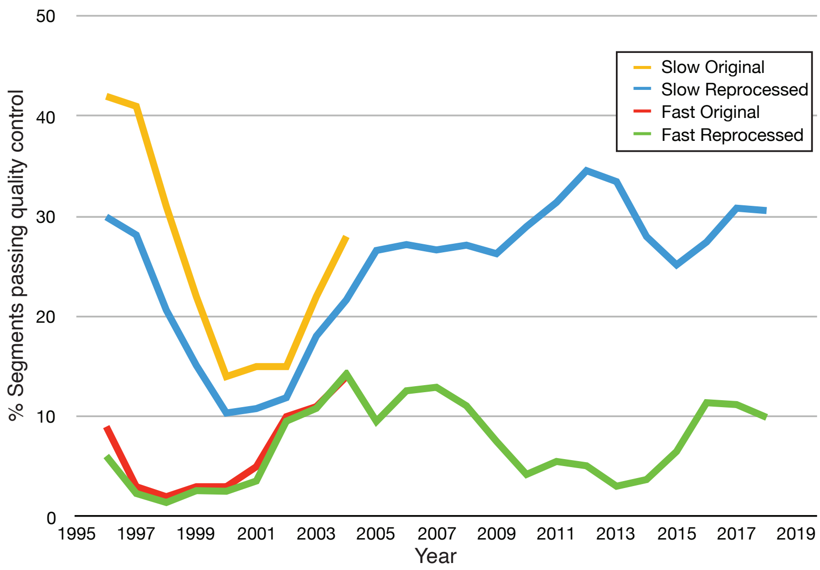

Figure 2. The percentage of the slow and fast solar wind length series segments that passed the quality control checks, and that were analyzed for periodic density structures. We also include the percentage of segments that passed these same quality checks in the original Viall et al. (2008) study. The differences are due to the reprocessed Wind SWE data.

pendent estimates of the spectra (Thomson, 1982). While producing a robust spectral estimate, this technique reduces the effective frequency resolution of the data as a function of the number of tapers chosen, K, to $2pf_R$, where $f_R = 1/(N\Delta L)$ is the Rayleigh frequency, and $p = (K+1)/2$. In this study we used 5 Slepian tapers, leading to an effective resolution of $6f_R$. We zeropad the data segments by a factor of 10 prior to calculating the spectral estimates. In Figure 3a and c we plot MTM spectra for the fast and slow length series segments shown in Figure 1, for both the original and reprocessed data. Note that the X-axis is in units of wavenumber Mm^{-1}, and we also list the equivalent length scale. Both the original and reprocessed data sets show similar spectral characteristics at the longer length scales (lower wavenumbers), but differ slightly at the smaller length scales (higher wavenumbers); the differences are more pronounced in the fast wind spectra. These trends are generally persistent across all segments, and is consistent with the reprocessed data having lower noise.

Viall et al. (2008), following Mann and Lees (1996), modeled the spectral background under the assumption that the observations x_i, at point t_i, followed an auto-regressive

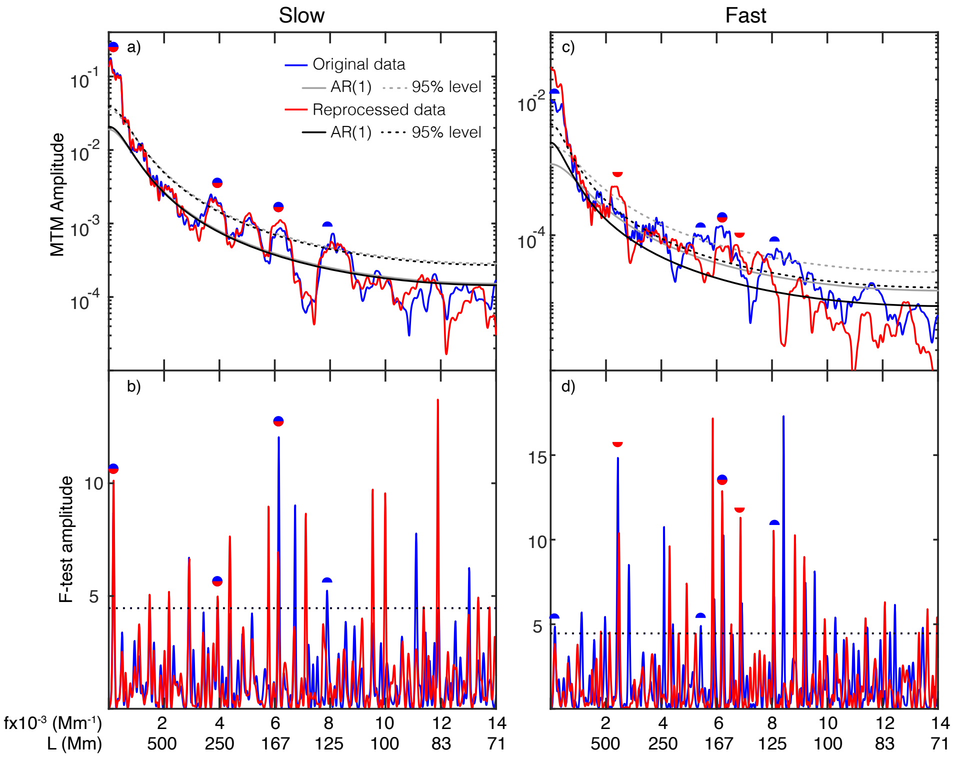

Figure 3. MTM spectra and f-test for both the slow (left) and fast (right) segment shown in Figure 1, and for both the original (blue) and reprocessed (red) Wind data. We have plotted an AR(1) background fit for both datasets, with the 95% confidence level. Peaks that simultaneously pass the amplitude and *f*-test are marked with half circles for both original (blue) and reprocessed (red) data.

AR(1) process, such that

$$x(t_i) = ax(t_{i-1}) + \epsilon_i \tag{1}$$

where a is the degree of correlation between sequential data points, and ϵ is random noise with zero mean (white noise). The limit of $a = 0$ produces a purely white noise spectrum, while larger values of a produce more strongly red-noise data series. The analytical spectrum of (1) is

$$S_{AR1}(f) = S_0 \frac{1 - a^2}{1 - 2a\cos(\pi f / f_N) + a^2} \tag{2}$$

where $S_0 = \sigma^2/(1-a^2)$ is the average value of the power spectrum, and σ^2 is the variance of the white-noise. We fit (2) to the spectra computed using the MTM to produce an estimation of the background under the assumption of red+white noise, and confidence levels are determined relative to that background. AR(1) background fits and 95%

confidence levels for the original and reprocessed datasets, for the fast and slow segments, are shown in Figure 3a and c, overlaid on the MTM amplitude spectra. The background AR(1) fit for both the original and reprocessed data are quite similar for the slow wind, with $a = 0.836$ and $a = 0.846$, respectively. For the fast wind, however, the spectra and AR(1) fits are quite different, due to reduced high frequency power in the reprocessed data, with $a = 0.792$ and $a = 0.883$ for the original and reprocessed data, respectively. For both fast and slow wind, the AR(1) background fits lie well above the background at shorter scales (higher wavenumber), suggesting AR(1) may not be a good background assumption. We return to this in the next section.

The determination of a significant spectral peak, in this example frequencies that have spectral power that exceed the 95% confidence threshold, is complicated by two issues. First, by definition power spectrum and confidence levels produce false positives at the rate determined by the confidence thresholds (Thomson, 1982; Mann & Lees, 1996). That is, for each frequency tested for significance, for a 95% test, e.g., there is a 5% probability of exceeding the threshold. These false positives would be randomly distributed in frequency, and therefore could not produce the types of preferential occurrence distributions identified by Viall et al. (2008). To minimize these "false positives", in addition to the amplitude test, we apply a second type of spectral test, the harmonic F-test, which is independent of the background fit (Mann & Lees, 1996). The amplitude test requires a signal to have strong power, but does not explicitly test the discrete nature of the power enhancement. On the other hand, the harmonic F-test tests for phase coherent signals, but does not test the power contained in those signals. As in Viall et al. (2008) we require that a spectral peak pass both the narrowband (amplitude) and F-test simultaneously to be considered significant and counted in our statistics. The precise value of the peak we identify is fixed to the maximum F-test frequency within the spectral amplitude band that exceeds the threshold. Because a peak has to pass both, independent, tests simultaneously at the 95% level, our confidence threshold in application is significantly higher than 95%. Assuming that the false positives from the two tests are uncorrelated, requiring that a signal pass both tests is analogous to testing at a 99.75% confidence threshold. The second issue in identifying significant spectarl peaks is that the choice of the background noise model, while not affecting the F-test, clearly affects the narrowband (amplitude) test, an issues we discuss below.

In Figure 3b and d we show the F-test for the representative segments, and we indicate peaks that pass both the narrowband and F-test at the 95% level with dots. Note that many peaks pass the harmonic F-test with little power, and are therefore not identified as significant in this combined test. Similarly, there are several amplitude peaks that exceed the amplitude threshold, but not the F-test. For example, the amplitude peak at $L = 200$ Mm in the slow wind, while significant in terms of spectral amplitude, was not considered phase coherent by the F-test, and therefore was not considered significant. Since the $F-$test is a test for phase coherence, our study likely undercounts solar wind signals that have significant power but are not precisely phase coherent. As such, results that use this technique should be considered a lower bound.

2.3 Background estimation

The narrowband (amplitude) spectral test is a measure of the power of a discrete signal relative to a background spectra. The AR(1) process assumption (Equation 1) is widely used, since it is reasonable to expect a physical system to have memory. However, whether that memory takes the precise from of the AR(1) in any particular segment of solar wind data is impossible to know *a priori*. Indeed, Figures 3a and c shows that the AR(1) does not fit the highest and lowest wavenumbers well. We find this to be a persistent characteristic of the AR(1) fit when applied to the solar wind number density data. In effect, this bias imposes a higher confidence threshold in order to pass, and indicates that the solar wind cannot be modeled as an AR(1) process over the ~ 6 hour windows we consider here.

The paleoclimatology community has studied the AR(1) background assumption extensively, where the choice of noise model impacts the ability to detect cycles in the stratigraphic record. In response to these concerns, Vaughan et al. (2011) suggest a bending power law (BPL) background spectrum fit

$$S_{BPL}(f) = \frac{N f^{-\beta}}{1 + (f/f_b)^{\gamma-\beta}} \tag{3}$$

which has the AR(1) as a special case, and performs well in mixed noise spectra. Here N is the normalization, β is the spectral slope index at low frequencies, γ is the spectral slope index at high frequencies, and f_b is the frequency at which the bend occurs. For low values of f_b, the BPL reduces to a straight power law with spectral slope $-\gamma$.

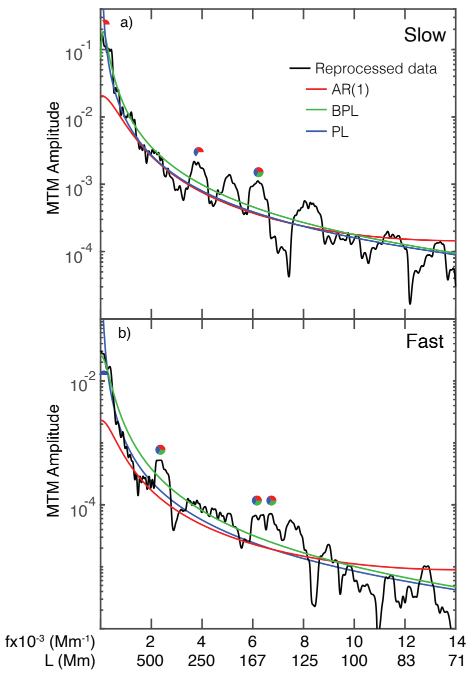

Figure 4. A comparison of three different background assumptions for the solar wind intervals shown in Figure 1. Shown are an AR(1) (red), a BPL (green) and power law (blue). We have not plotted the 95% confidence levels for clarity. Peaks that simultaneously pass the amplitude and f-test at 95 % are marked for the different fits. The spectral background model parameters are $N = 24.33$, $\beta = -0.51$, $\gamma = 1.87$, $f_b = 1.8 \times 10^{-4}$ Mm^{-1} for BPL slow wind; $p = -1.74$ for PL slow wind; $N = .02$, $\beta = .02$, $\gamma = 2.26$, $f_b = 3.2 \times 10^{-4}$ for BPL fast wind; $p = -2.1$ for PL fast wind.

The BPL fit, and the 95% confidence level, is shown in Figure 4a and b in green for the same segments shown in Figure 3. Note how the BPL is a better representation of the background at both the higher and lower wavenumbers compared to AR(1) (red). We also plot a straight power law (blue) with spectral slope, p, for both slow and fast segments for reference. There is consistency in the identified peaks using the different background assumptions, with the BPL assumption producing fewer peaks in the slow wind segment. This tendency for BPL to identify fewer significant peaks than AR(1), particularly at lower frequencies, is a consistent feature across the entire 25-year study.

The BPL is flexible in that it allows for an AR(1) solution, a single power law, and a host of solutions in between. Since the BPL approximates the solar wind background spectra better than AR(1), and because it is more versatile than a straight power law, we utilize BPL as one of the two background assumptions we use for our statistical study. For consistency with Viall et al. (2008) we also run the analysis with an AR(1) background estimate.

2.4 Occurrence Distributions

We applied the data processing and spectral analysis methods described above to the reprocessed solar wind measured by the Wind spacecraft from 1995-2019. For each segment we determine statistically significant peaks that pass the amplitude and F-tests simultaneously, for both BPL and AR(1) background assumptions. We create separate occurrence distributions (ODs) of the statistically significant lengths (inverse wavenumbers) identified using the AR(1)+F-test and BPL+F-test criteria. For each set, we compute occurrence distributions over overlapping, three-year intervals, with bins of width $6\lambda_R$, the effective resolution of the MTM with our choice of $K = 5$, stepping by $3\lambda_R$ for each subsequent bin. For each 3-year window, we applied the bootstrap technique ($N = 500$) to estimate the uncertainty of local peaks on the histogram, and calculated a median histogram, median fit, and standard deviation from these 500 instantiations.

To demonstrate this process we show the median histograms, representing an occurrence distribution, for 1995-1998 for both the fast and slow solar wind in Figure 5a and b, with 2σ standard deviation bars determined via the bootstrap method (Efron & Tibshirani, 1993). Visually, these histograms exhibit locally enhanced counts for particular lengthscale bands, with strong correlation between the occurrence enhancements using the AR(1) and BPL background fits. The residuals (Figure 5b and d) highlight the similarity in local occurrence enhancements between the AR(1) and BPL histograms, despite the differences in the overall shape of the occurrence distributions. We use the bootstrapped occurrence distributions to determine statistically significant occurrence enhancements as those points that are $> 2\sigma$ above the background fit. These are highlighted with circle in Figures 5b and d, and with thick lines in Figure 5a and c.

Importantly, although the AR(1) and BPL background models produce different overall shapes of the occurrence distributions, they produce similar residuals, and similar occurrence enhancements are identified as statistically significant with the bootstrap method for each. For the slow wind, the OD determined with the AR(1) assumption exhibits a steep slope on the short length scale (higher wavenumber) end, consistent with

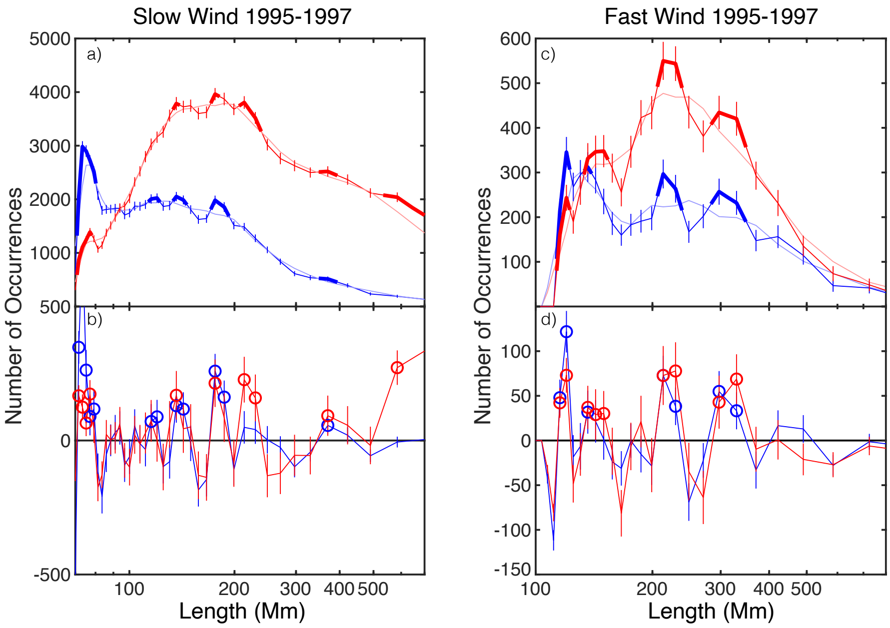

Figure 5. 3-year occurrence distributions for 1995-1997 for the slow and fast solar wind calculated for both the AR(1) (red) and BPL (blue) spectral background assumptions. Vertical bars represent $\pm 2\sigma$ standard deviation. Length scales that are greater than 2σ above the median fit (dashed lines) are shown in thick lines in (a) and (c), where we have extended the significant length scale range by $f_R/2$ in either direction. The residual distributions, obtained by subtracting the median fits from the occurrence distributions, are shown in (b) for the slow and (d) for the fast wind. Circles denote points that exceed 2σ.

the examples shown in Figures 3 and 4. The BPL assumption does not exhibit this bias, which provides confidence for local occurrence enhancements within this region (between $\sim 90 - 150$ Mm). For example, there is a local occurrence enhancement identified in the BPL OD near 110 Mm as $> 2\sigma$ significant, on top of a relatively flat part of the distribution. In the AR(1) OD, this shows up as a relatively small local enhancement, and appears in the residual histogram as well, but is not significant at the 2σ level. In addition, the ODs produced with the BPL assumption identify $\sim$ 50% fewer significant peaks than those with the AR(1) assumption. This trend is consistent throughout the 25-year interval, and indicates that the BPL is likely a better approximation for the solar wind background spectra, with fewer false positive detections. Despite the difference between the AR(1) and BPL results in absolute counts, the relative amplitude of the enhancements in the occurrence distribution are similar between the two background model assumptions.

3 Results

We ran the entire 25 year Wind SWE dataset through the analysis process described in Section 2. Figure 6 shows the percentage of analyzed segments that contained at least 1 statistically significant peak that simultaneously passed the amplitude and F-test at the 95% confidence levels, for each of the AR(1) and BPL background assumptions, compared to the Viall et al. (2008) study. Viall et al. (2008), using the original Wind data, showed an increasing trend with time of the fraction of segments containing $\geq$ 1 statistically significant frequency. This trend does not appear in the reprocessed data. Instead, there is a relatively consistent number of significant radial-length peaks identified in segments during the 25-year interval, with the BPL background assumption producing consistently fewer statistically significant peaks than AR(1).

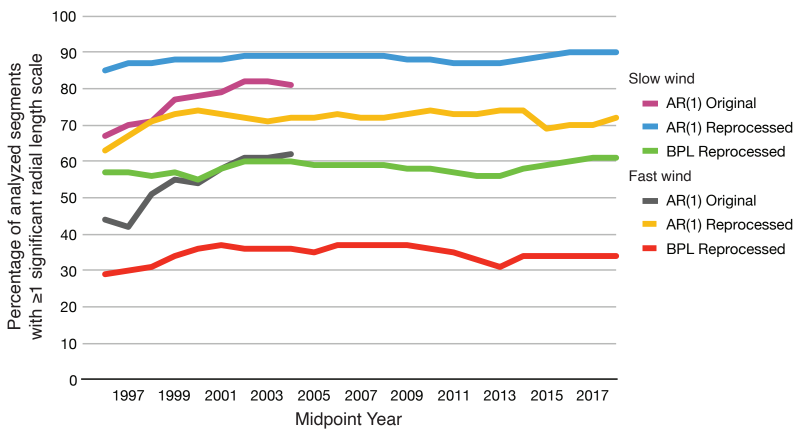

Figure 6. The percentage number of segments containing $\geq$1 statistically significant length scale for the two different fits, for both fast and slow wind, compared to the results of Viall et al. (2008)

We show in Figure 7 the normalized occurrence distributions of statistically significant radial length scales for slow and fast wind, and for both the AR(1) and BPL background assumptions, for all 25 years of Wind data. We computed the histograms in 3-year intervals, shifting by 1-year for each new histogram. We mark the occurrence enhancements (i.e. the persistent length scales) that are $> 2\sigma$ above the occurrence distribution with thick lines in Figure 7. For example, the histograms for 2017-2019 slow wind in Figure 7 show in the BPL histogram 3 clear peaks below 100 Mm, and two broad peaks near 130 and 160 Mm. The histogram derived from the AR(1) assumption show the first 2 peaks below 100 Mm and the two broad peaks near 130 and 160 Mm, but at a reduced relative amplitude compared to the BPL histogram.

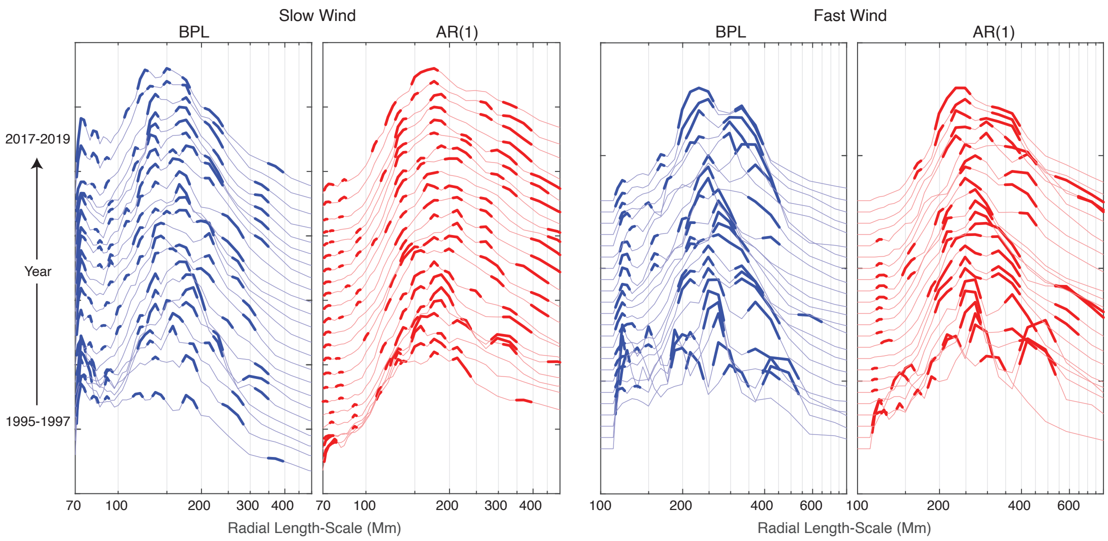

Figure 7. Bootstrapped occurrence distributions of length scales identified as significant by passing both the amplitude and F-test at the 95% level, for both slow (left) and fast (right) wind, and both background assumptions. Local peaks that exceed the background by 2σ are considered significant and are marked with thick lines.

To compare between the two background assumptions, we plot the significant length scales identified in both the AR(1) and BPL derived occurrence distributions as significant at the 2σ level as horizontal bars in Figure 8. This comparison shows that the method applied with both background model assumptions resulted in the very similar length-scales identified as occurrence enhancements in the distributions. The primary differences are at the ends of the spectral range analyzed, and follow the general pattern identified in the example shown in Figure 4. At the long length-scale end (low wavenumber), fewer significant peaks were identified with the BPL (blue) background assumption, while at the short-length-scale end (high wavenumber), fewer peaks were identified with the AR(1) (red) background assumption. Many of the occurrence distributions exhibit local enhancements at the smallest length scales, very near the Nyquist, and therefore we shade those particular length scales lighter to emphasize they may not be significant. Lengths that were identified concurrently in the occurrence distributions of both model fits are shown in Figure 8 as solid black bars.

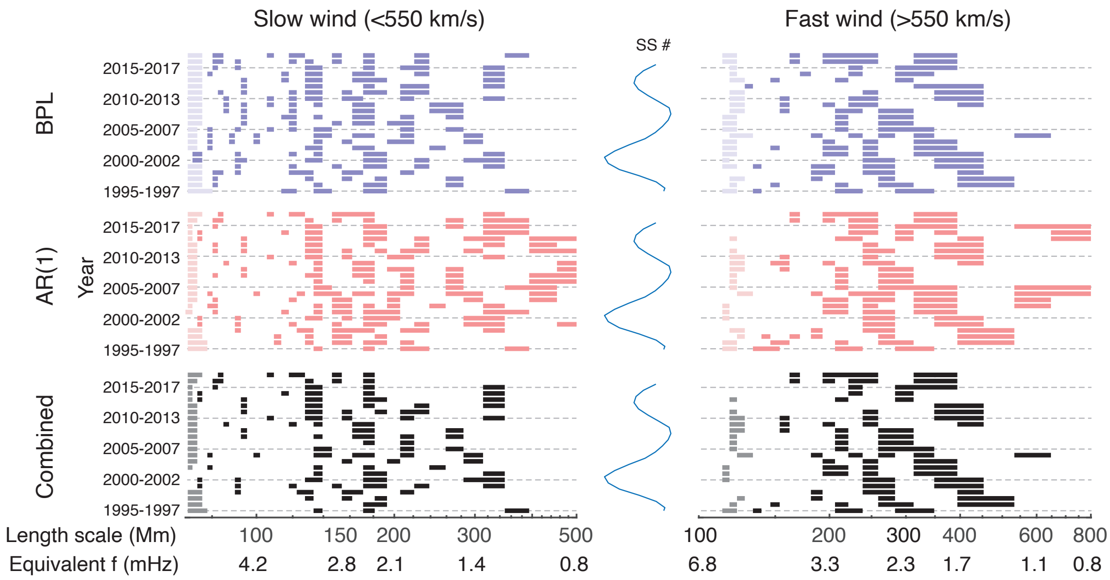

Figure 8. Bars represent statistically significant length scales identified in the occurrence distributions of Figure 7 as above the background at the 2σ level. Length scales at edge of the OD that may be affected by the Nyquist are lightly shaded. Black bars represent length scales identified simultaneously in both BPL and AR(1)distributions. We also show the equivalent frequencies using the median solar wind speed of 420 km/s for slow, and 675 for fast. For Earth's magnetosphere, or an in situ spacecraft, these length scales would appear as periodicities at these frequencies. The sunspot number cycle is shown in the middle for reference.

The new results are consistent with the previous results of Viall et al. (2008) that covered the years 1995-2005 using the original Wind data. Figure 9 shows the concurrently identified significant length scales from Figure 8 with the AR(1) derived results from Viall et al. (2008). For the slow wind (Figure 9a), both studies identified significant lengths near 130 and 170 Mm, and an additional set near 330 Mm. The differences between the original and reprocessed data occur primarily in the first 3 rows, covering years 1995-2001, during the earliest portion of the Wind mission. The fast wind results compare very well to the previous Viall et al. (2008) results, with 3 sets of length scales near 100, 300, and 400-500 Mm detected in both the original and reprocessed Wind data. The slight shift to shorter length scales in the 80-500 Mm bands in the reprocessed data results is due to a reduced central peak in the OD in the reprocessed data compared to the original data.

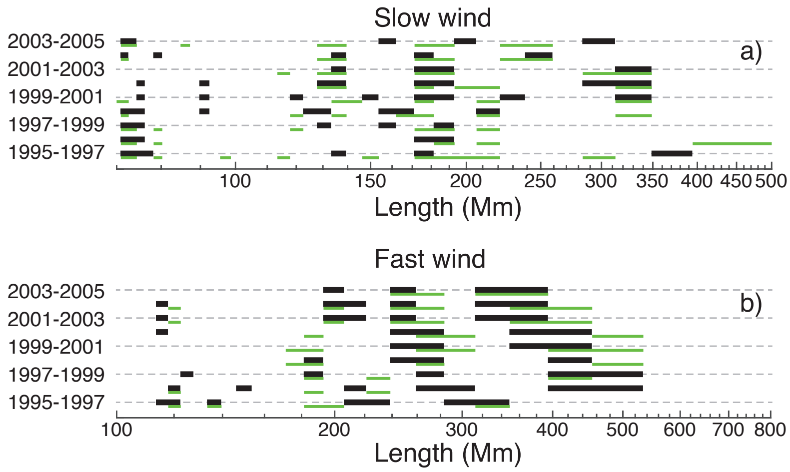

Figure 9. Comparison between the statistically significant length scales identified by Viall et al. (2008) (green) and this study (black).

4 Discussion

The histograms shown in Figure 7 represent occurrence distributions of significant length scales observed in the solar wind near L1 over 2 solar cycles. The overall shape of these distributions exhibits a consistent pattern across the full 25 years of Wind data (Figure 7). For the slow wind, the statistically significant length scales identified using the BPL background assumption exhibit comparatively few counts at the longer length scales (> 300 Mm), and a broad peak near the center of the distribution (100-200 Mm). The AR(1)-derived histograms exhibit a steep slope at the smaller length scales, followed by a slow decline at the longer length scales. The histograms for the fast wind length scales show a similar, although less pronounced, trend. Future work examining longer data segments is required to understand the nature of the shape of the occurrence distribution over these length scales.

In addition to these overall trends, the occurrence distributions exhibit local enhancements of length scales identified as significant. These are highlighted in the occurrence distribution histograms in Figure 7 and pulled out separately in Figure 8 as bars. Figures 7 and 8 together provide evidence for persistent bands of significant periodic length scales. To highlight these trends we have plotted colored contour plots, along with the normalized residuals from which these length scales were determined, in Figure 10a and 10b. The residuals here are the addition of the normalized occurrence distribution residuals from the BPL and AR(1) background assumptions. The plotted values are $(OD_{BPL} - fit_{BPL}) + (OD_{AR(1)} - fit_{AR(1)})$, where OD is the 3-year occurrence distribution and fit is the occurrence distribution fit for the two spectral background assumptions. Length scale occurrence enhancements that were detected in both occurrence distribution residuals would add together (red), while parts of the distributions that are less correlated would tend to zero (green).

Figure 10a and 10b shows clear patterns of periodic length scales that evolve over the full 25 years of Wind SWE data. In the slow wind, $L \sim 90$ Mm (VI), $L \sim 130-140$ Mm (III), and $L \sim 170-190$ Mm (II), are all observed for the majority of the 25-year dataset, with some noticeable variations we discuss below. There are two smaller bands near $L \sim 210$ Mm (IV) in the middle years and between 310 and 350 Mm in the later years, and a sloped band between 250 and 400 Mm (I) for the first half of the interval. An additional band appears near $L \sim 120$Mm in the BPL-derived histograms in Figure 7a, but is not apparent in the AR(1)-derived histograms, likely because this region has a very strong slope; there is a similar effect with the $L \sim 90$ Mm band (see Figure 7). For the fast wind there is an intermittent band between $L \sim 200-220$ Mm (IV), and a series of sloped bands that appear to decrease in L as functions of year.

Figure 10c shows a pictorial summary of the significant length scale bands, derived by examining the combined bar plots and residual contours of Figure 10a and 10b, and using the additional information of the histograms in Figure 7 to provide visual guidance on persistence. We have also combined the significant length scales observed in the slow and fast wind together. We note that bands I, IV and V, observed in both fast and slow wind analysis, clearly overlap, suggesting that these periodic density structures are not a strictly "slow" (< 550 km/s) wind phenomenon.

Many characteristics of the Sun, solar corona, and solar wind are correlated with solar cycle, so unraveling the specific nature of the correlation of periodic density structures with solar cycle is a topic for future work. Here we speculate on a likely connection. In general, the solar corona is hotter, and its magnetic topology increases in complexity, at solar maximum, as manifested in active regions and their underlying magnetic concentrations, sunspots. To the right of Figure 10c we show the gradual solar cycle change as measured by 3-year averages of the sunspot number, along with the more abrupt "terminator" events that occur during the rising phase of the solar cycle (McIntosh et al., 2015, 2019). The terminator events are observed as abrupt changes in the distribution of solar EUV bright points, and are correlated with the appearance of active regions (and their associated sunspots) that have the polarity of the next solar cycle. Active regions with the past-cycle polarity can occur even after solar minimum, hence these terminator events are offset in time from sunspot minimum. Related, Schonfeld et al. (2017) showed that the amount of hot plasma (plasma greater than $10^{6.1}$K) in the solar corona abruptly increases at the terminator, due to an increased amount of hot plasma in active regions.

The length scale bands that we find in this paper exhibit a solar cycle dependence, but they exhibit breaks that are associated more closely with terminators than with sunspot minimum. For example, bands I and II at both ends, and band III for the termination event of solar cycle 22. Additionally, there is a gradual evolution of the characteristic length scales between termination events, most pronounced in bands I and V. With data from only two, very different, solar cycles, we cannot draw definitive conclusions about the exact relationship between solar wind periodic length scales and the solar cycle, but the result suggests that a relationship exists.

As reviewed in Section 1, there is strong evidence that periodic density structures originate from the sun and are associated with magnetic reconnection of plasma from closed-field regions. The association of periodic length scales with solar cycle could be the result of changes in the nature of the interchange reconnection that releases the plasma into the solar wind, due to the increase in complexity of the global magnetic topology (Antiochos et al., 2011) and the local nature of the magnetic field concentrations (Mason et al., 2019). Coronal temperature is correlated with solar wind speed, so it could also be that the hotter active regions accelerate solar wind, and any embedded periodic density structures, differently.

While this study focused specifically on mesoscale structures measured at L1 that exhibit periodicity in density, many other studies have observed mesoscale structures in the solar wind that form at the sun and advect to 1 AU. A general picture is emerging in which mesoscale structures that form through spatial structures that rotate (Borovsky, 2008, 2020) or time dynamics such as reconnection in the corona (Sanchez-Diaz et al., 2016, 2017, 2019; M. J. Owens et al., 2018; M. Owens et al., 2020; Stansby & Horbury, 2018), are an inherent part of solar wind formation (see review by Viall and Borovsky, 2010).

In a series of papers, Rouillard, Davies, et al. (2010), Rouillard, Lavraud, et al. (2010), and Rouillard et al. (2011) tracked larger mesoscale structures from their formation in the corona through the inner heliosphere using SECCHI HI images, all the way to their impact at the Earth. They identified the corresponding compositional and magnetic field variations inherent to the structures, which were retained out to 1 AU. This set of studies unequivocally demonstrated that mesoscale structures created at the Sun survive to 1 AU with identifiable in situ signatures. More recently, Rouillard et al. (2020) tracked density structures through the STEREO COR2 and HI1 FOVs to their impact at Parker Solar Probe, where they observed a one-to-one correlation between the $\sim 3-4$ hour density structures observed remotely and the in situ Parker measurements. They showed that Parker measured additional sequences of small density peaks separated in time by approximately 90-120 minutes, suggestive of the types of periodic density enhancements at 90 minute timescales that have been observed in situ at L1 (Viall et al., 2008; Kepko & Spence, 2003), near Mercury's orbit with Helios (Matteo et al., 2019) and remotely with STEREO (Viall & Vourlidas, 2015). Many of these event studies exhibited still smaller substructures at tens of minutes (Matteo et al., 2019; Kepko & Viall, 2019; Stansby & Horbury, 2018; Kepko & Spence, 2003). Several studies also found composition signatures which could only have come from formation at the sun (Viall, Spence, & Kasper, 2009; Kepko & Viall, 2019). These studies together demonstrate that the solar wind is often composed of mesoscale density structures, and provide ample evidence that structures of order tens of minutes timescales and longer form with the solar wind and survive through the inner heliosphere, out to 1 AU. This current study further demonstrated that at least some of those structures are quasi periodic, and occur at repeatable sets of frequencies and/or length scales.

We emphasize that these length scales represent periodic density structures that advect with the solar wind. In the rest frame of a spacecraft or planet, they would appear as a periodic density variations at a frequency determined by $f_{PDS} = V_{sw}/L_{PDS}$. Statistically, for any particular year the magnetosphere or a spacecraft would see a spectrum of equivalent frequencies determined by convolving the distribution of solar wind V_x with the length scales identified in Figures 8 and 10c from that year. To zeroth order, we can estimate these frequencies using the median solar wind speed for "fast" and "slow" solar wind. These equivalent frequencies are listed at the bottom of Figure 10c. The equivalent frequencies of these structures fall in the few mHz range, which for the magnetosphere is considered the Pc5 band and higher. Previously, Viall, Kepko, and Spence (2009) studied 11 years of Wind SWE data covering 1995-2005 for evidence of discrete frequency periodicities in the solar wind number density. They found that $f = 0.7$, $1.3-1.5$, $2.0-2.3$, and $4.7-4.8$ mHz occurred most often over that 11-year interval. Figure 10c demonstrates that $f = 1.4$ mHz corresponds to Band I in the slow wind, $f = 2.0-2.3$ mHz corresponds to Band IV in the slow and I in the fast, and $f = 4.7-4.8$ mHz corresponds to Band VI in the slow wind.

Since these are periodic structures in solar wind density, they would periodically compress the magnetosphere via periodic dynamic pressure changes, and we would expect the magnetosphere to show these same sets of frequencies. In the same Viall, Kepko, and Spence (2009) study, they also examined GOES magnetospheric magnetic field data for intervals when GOES was near the dayside magnetopause, and found in the GOES data a similar set of frequencies to those found in the solar wind. In a direct comparison between Wind and GOES, they found when a spectral peak was observed in the solar wind, that same peak was observed at GOES 54% of the time. Other statistical studies have similarly identified persistent bands of significant mHz frequencies (e.g., Francia and Villante (1997); Chisham and Orr (1997); Ziesolleck and McDiarmid (1995)). While originally attributed to global cavity modes (e.g., Harrold and Samson (1992)), we now know these $<\sim 4$ mHz oscillations are largely driven by solar wind periodic density structures. Since these periodic length scales directly drive the magnetosphere, we would expect the spectrum of discrete mHz oscillations in the magnetosphere to vary year-to-year as the L_{PDS} vary. Since the L_{PDS} have a solar cycle dependence, this would mean the spectrum of discrete mHz waves in the magnetosphere would also have a solar cycle dependence, although the variability of the solar wind speed would produce broad, rather than narrow, enhancements. This slow year-to-year variability, and the distribution of solar wind speeds, can explain year-to-year changes in measured frequencies. In addition, Kepko and Viall (2019), showed that ambient periodic density structures in the slow solar wind were sometimes compressed and amplified by a faster solar wind stream from behind, and that these amplified PDSs had an observable impact on radiation belt particles. These particular PDSs were observed with stream interaction regions, which are known to be important drivers of radiation belt flux enhancements.

5 Conclusions

Using 25 years of Wind solar wind number density data observed near L1 we have identified bands of periodic length scales that occur more often than others. Each occurrence of periodic length scales passed two independent spectral tests at the 95% level, and we tested each occurrence with two different background spectral models. We identify bands of occurrence enhancements that are persistent in time, and regardless of background spectral model (Figure 8c). These bands, particularly at larger length scales, have a clear solar cycle dependence, and their evolution may be related to "terminator" events (Figure 10). This study provides further evidence that large portions of the solar wind plasma consist of mesoscale structures that are released via magnetic reconnection. Finally, in the rest frame of a spacecraft or Earth, these periodic mesoscale density structures would appear as Pc5-6 pulsations, which are known to be important in processes leading to radiation belt particle loss, diffusion, and acceleration. Given the statistical bands of recurrent length scales in the solar wind, and a solar cycle dependence, it may be possible in the future to produce a statistical model for these solar-wind driven discrete oscillations.

Acknowledgments

L. Kepko and N. Viall acknowledge the Heliophysics Internal Scientist Funding Model and the NASA Guest Investigator program for funding. K. Wolfinger was supported through the NASA internship program. All data used in this study were obtained from CDAWeb `https://cdaweb.sci.gsfc.nasa.gov/`.

References

Antiochos, S. K., Miki, Z., Titov, V. S., Lionello, R., & Linker, J. A. (2011). A MODEL FOR THE SOURCES OF THE SLOW SOLAR WIND. *The Astrophysical Journal*, *731*(2), 112. Retrieved from `http://iopscience.iop.org/0004-637X/731/2/112` doi: 10.1088/0004-637x/731/2/112

Borovsky, J. E. (2008). Flux tube texture of the solar wind: Strands of the magnetic carpet at 1 AU? *Journal of Geophysical Research: Space Physics (19782012)*, *113*(A8), n/a–n/a. doi: 10.1029/2007ja012684

Borovsky, J. E. (2012). The velocity and magnetic field fluctuations of the solar wind at 1 AU: Statistical analysis of Fourier spectra and correlations with plasma properties. *Journal of Geophysical Research: Space Physics (19782012)*, *117*(A5). doi: 10.1029/2011ja017499

Borovsky, J. E. (2020). The Magnetic Structure of the Solar Wind: Ionic Composition and the Electron Strahl. *Geophysical Research Letters*, *47*(5). doi: 10.1029/2019gl084586

Chisham, G., & Orr, D. (1997). A statistical study of the local time asymmetry of Pc 5 ULF wave characteristics observed at midlatitudes by SAMNET. *Journal of Geophysical Research: Space Physics*, *102*(A11), 24339–24350. doi: 10.1029/97ja01801

DeForest, C. E., Howard, R. A., Velli, M., Viall, N., & Vourlidas, A. (2018). The Highly Structured Outer Solar Corona. *The Astrophysical Journal*, *862*(1), 18. doi: 10.3847/1538-4357/aac8e3

DeForest, C. E., Matthaeus, W. H., Viall, N. M., & Cranmer, S. R. (2016). FADING CORONAL STRUCTURE AND THE ONSET OF TURBULENCE IN THE YOUNG SOLAR WIND. *The Astrophysical Journal*, *828*(2), 66. doi: 10.3847/0004-637x/828/2/66

Dyrud, L. P., Behnke, R., Kepko, E. L., Sulzer, M., & Zafke, S. (2008). Ionospheric ULF oscillations driven from above Arecibo. *Geophysical Research Letters (ISSN 0094-8276)*, *35*(14). doi: 10.1029/2008gl034073

Efron, B., & Tibshirani, R. J. (1993). An Introduction to the Bootstrap. doi: 10.1007/978-1-4899-4541-9

Fenrich, F. R., & Waters, C. L. (2008). Phase coherence analysis of a field line resonance and solar wind oscillation. *Geophysical Research Letters (ISSN 0094-8276)*, *35*(20), 4. Retrieved from `http://adsabs.harvard.edu/cgi-bin/nph-data\_query?bibcode=2008GeoRL..3520102F\&link\_type=ABSTRACT` doi: 10.1029/2008gl035430

Francia, P., Lanzerotti, L. J., Villante, U., Lepidi, S., & Memmo, D. D. (2005). A statistical analysis of lowfrequency magnetic pulsations at cusp and cap latitudes in Antarctica. *Journal of Geophysical Research: Space Physics (19782012)*, *110*(A2). doi: 10.1029/2004ja010680

Francia, P., & Villante, U. (1997). Some evidence of ground power enhancements at frequencies of global magnetospheric modes at low latitude. *Annales Geophysicae*, *15*(1), 17–23. Retrieved from `http://adsabs.harvard.edu/cgi-bin/nph-data\_query?bibcode=1997AnGeo..15...17F\&link\_type=ABSTRACT` doi: 10.1007/s00585-997-0017-2

Harrold, B. G., & Samson, J. C. (1992). Standing ULF modes of the magnetosphere: A theory. *Geophysical Research Letters*, *19*(18), 1811–1814. Retrieved from `http://onlinelibrary.wiley.com/doi/10.1029/92GL01802/full` doi: 10.1029/92gl01802

Hartinger, M. D., Angelopoulos, V., Moldwin, M. B., Takahashi, K., & Clausen, L. B. N. (2013). Statistical study of global modes outside the plasmasphere. *Journal of Geophysical Research: Space Physics*, *118*(2), 804–822. doi: 10.1002/jgra.50140

Hollweg, J. V., Verscharen, D., & Chandran, B. D. G. (2014). Magnetohydrodynamic Slow Mode with Drifting He$ˆ{++}$: Implications for Coronal Seismology and the Solar Wind. *The Astrophysical Journal*, *788*(1), 35. doi: 10.1088/0004-637x/788/1/35

Kasper, J. C., Lazarus, A. J., Steinberg, J. T., Ogilvie, K. W., & Szabo, A. (2006). Physics-based tests to identify the accuracy of solar wind ion measurements: A case study with the Wind Faraday Cups. *Journal of Geophysical Research*, *111*(A3). doi: 10.1029/2005ja011442

Kepko, L., & Spence, H. E. (2003). Observations of discrete, global magnetospheric oscillations directly driven by solar wind density variations. *Journal of Geophysical Research: Space Physics (19782012)*, *108*(A6), 1257. doi: 10.1029/2002ja009676

Kepko, L., Spence, H. E., & Singer, H. J. (2002). ULF waves in the solar wind as direct drivers of magnetospheric pulsations. *Geophysical Research Letters*, *29*(8), 39 1. doi: 10.1029/2001gl014405

Kepko, L., & Viall, N. M. (2019). The Source, Significance, and Magnetospheric Impact of Periodic Density Structures Within Stream Interaction Regions. *Journal of Geophysical Research: Space Physics*. doi: 10.1029/2019ja026962

Kepko, L., Viall, N. M., Antiochos, S. K., Lepri, S. T., Kasper, J. C., & Weberg, M. (2016). Implications of L1 observations for slow solar wind formation by solar reconnection. *Geophysical Research Letters*, *43*(9), 4089–4097. doi: 10.1002/2016gl068607

Mann, M. E., & Lees, J. M. (1996). Robust estimation of background noise and signal detection in climatic time series. *Climatic Change*, *33*(3), 409–445. doi: 10.1007/bf00142586

Mason, E. I., Antiochos, S. K., & Viall, N. M. (2019). Observations of Solar Coronal Rain in Null Point Topologies. *The Astrophysical Journal*, *874*(2), L33. doi: 10.3847/2041-8213/ab0c5d

Mathie, R. A., Mann, I. R., Menk, F. W., & Orr, D. (1999). Pc5 ULF pulsations associated with waveguide modes observed with the IMAGE magnetometer array. *Journal of Geophysical Research: Space Physics*, *104*(A4), 7025. Retrieved from `http://adsabs.harvard.edu/cgi-bin/nph-data\_query?bibcode=1999JGR...104.7025M\&link\_type=ABSTRACT` doi: 10.1029/1998ja900150

Matteo, S. D., Viall, N. M., Kepko, L., Wallace, S., Arge, C. N., & MacNeice, P. (2019). Helios Observations of Quasiperiodic Density Structures in the Slow Solar Wind at 0.3, 0.4, and 0.6 AU. *Journal of Geophysical Research: Space Physics*, *124*(2), 837–860. doi: 10.1029/2018ja026182

McIntosh, S. W., Leamon, R. J., Egeland, R., Dikpati, M., Fan, Y., & Rempel, M. (2019). What the Sudden Death of Solar Cycles Can Tell Us About the Nature of the Solar Interior. *Solar Physics*, *294*(7), 88. doi: 10.1007/s11207-019-1474-y

McIntosh, S. W., Leamon, R. J., Krista, L. D., Title, A. M., Hudson, H. S., Riley, P., … Ulrich, R. K. (2015). The solar magnetic activity band interaction and instabilities that shape quasi-periodic variability. *Nature Communications*, *6*(1), 6491. doi: 10.1038/ncomms7491

Ogilvie, K. W., Chornay, D. J., Fritzenreiter, R. J., Hunsaker, F., Keller, J., Lobell, J., … Gergin, E. (1995). SWE, A Comprehensive Plasma Instrument for the Wind Spacecraft. *Space Science Reviews*, *71*(1), 55 77. doi: 10.1007/bf00751326

Owens, M., Lockwood, M., Macneil, A., & Stansby, D. (2020). Signatures of Coronal Loop Opening via Interchange Reconnection in the Slow Solar Wind at 1 AU. *Solar Physics*, *295*(3), 37. doi: 10.1007/s11207-020-01601-7

Owens, M. J., Lockwood, M., Barnard, L. A., & MacNeil, A. R. (2018). Generation of Inverted Heliospheric Magnetic Flux by Coronal Loop Opening and Slow Solar Wind Release. *The Astrophysical Journal*, *868*(1), L14. doi: 10.3847/2041-8213/aaee82

Roberts, D. A., Karimabadi, H., Sipes, T., Ko, Y.-K., & Lepri, S. (2020). Objectively Determining States of the Solar Wind Using Machine Learning. *The Astrophysical Journal*, *889*(2), 153. doi: 10.3847/1538-4357/ab5a7a

Rouillard, A. P., Davies, J. A., Lavraud, B., Forsyth, R. J., Savani, N. P., Bewsher, D., … Eyles, C. J. (2010). Intermittent release of transients in the slow solar wind: 1. Remote sensing observations. *Journal of Geophysical Research: Space Physics (19782012)*, *115*(A4), n/a–n/a. doi: 10.1029/2009ja014471

Rouillard, A. P., Kouloumvakos, A., Vourlidas, A., Kasper, J., Bale, S., Raouafi, N.-E., … Penou, E. (2020). Relating streamer flows to density and magnetic structures at the Parker Solar Probe. *The Astrophysical Journal Supplement Series*, *246*(2), 37. doi: 10.3847/1538-4365/ab579a

Rouillard, A. P., Lavraud, B., Davies, J. A., Savani, N. P., Burlaga, L. F., Forsyth, R. J., … Harrison, R. A. (2010). Intermittent release of transients in the slow solar wind: 2. In situ evidence. *Journal of Geophysical Research: Space Physics (19782012)*, *115*(A4), n/a–n/a. doi: 10.1029/2009ja014472

Rouillard, A. P., Sheeley, N. R., Cooper, T. J., Davies, J. A., Lavraud, B., Kilpua, E. K. J., … Sauvaud, J. A. (2011). THE SOLAR ORIGIN OF SMALL INTERPLANETARY TRANSIENTS. *The Astrophysical Journal*, *734*(1), 7. doi: 10.1088/0004-637x/734/1/7

Saito, T. (1978). Long-period irregular magnetic pulsation, Pi3. *Space Science Reviews*, *21*(4), 427–467. doi: 10.1007/bf00173068

Sanchez-Diaz, E., Rouillard, A., Lavraud, B., Kilpua, E., & Davies, J. (2019). In situ measurements of the variable slow solar wind near sector boundaries. *The Astrophysical Journal*, *882*(1), 51. doi: 10.3847/1538-4357/ab341c

Sanchez-Diaz, E., Rouillard, A. P., Davies, J. A., Lavraud, B., Pinto, R. F., & Kilpua, E. (2017). The temporal and spatial scales of density structures released in the slow solar wind during solar activity maximum. *The Astrophysical Journal*, *851*(1), 32. doi: 10.3847/1538-4357/aa98e2

Sanchez-Diaz, E., Rouillard, A. P., Davies, J. A., Lavraud, B., Sheeley, N. R., Pinto, R. F., ... Genot, V. (2016). Observational evidence for the associated formation of blobs and raining inflows in the solar Corona. *The Astrophysical Journal*, *835*(1), L7. doi: 10.3847/2041-8213/835/1/l7

Schonfeld, S. J., White, S. M., Hock-Mysliwiec, R. A., & McAteer, R. T. J. (2017). The Slowly Varying Corona. I. Daily Differential Emission Measure Distributions Derived from EVE Spectra. *The Astrophysical Journal*, *844*(2), 163. doi: 10.3847/1538-4357/aa7b35

Stansby, D., & Horbury, T. S. (2018). Number density structures in the inner heliosphere. *Astronomy & Astrophysics*, *613*, A62. doi: 10.1051/0004-6361/201732567

Stephenson, J. A. E., & Walker, A. D. M. (2002). HF radar observations of Pc5 ULF pulsations driven by the solar wind. *Geophysical Research Letters*, *29*(9), 8–1-8-4. doi: 10.1029/2001gl014291

Takahashi, K., & Ukhorskiy, A. Y. (2007). Solar wind control of Pc5 pulsation power at geosynchronous orbit. *Journal of Geophysical Research: Space Physics (19782012)*, *112*(A11), n/a–n/a. doi: 10.1029/2007ja012483

Thomson, D. (1982). Spectrum estimation and harmonic analysis. *Proceedings of the IEEE*, *70*(9), 1055–1096. doi: 10.1109/proc.1982.12433

Vaughan, S., Bailey, R. J., & Smith, D. G. (2011). Detecting cycles in stratigraphic data: Spectral analysis in the presence of red noise. *Paleoceanography*, *26*(4). doi: 10.1029/2011pa002195

Viall, N. M., Kepko, L., & Spence, H. E. (2008). Inherent lengthscales of periodic solar wind number density structures. *Journal of Geophysical Research: Space Physics*, *113*(A7), n/a–n/a. doi: 10.1029/2007ja012881

Viall, N. M., Kepko, L., & Spence, H. E. (2009). Relative occurrence rates and connection of discrete frequency oscillations in the solar wind density and dayside magnetosphere. *Journal of Geophysical Research: Space Physics (19782012)*, *114*(A1), n/a–n/a. doi: 10.1029/2008ja013334

Viall, N. M., Spence, H. E., & Kasper, J. (2009). Are periodic solar wind number density structures formed in the solar corona? *Geophysical Research Letters (ISSN 0094-8276)*, *36*(23), 23102. doi: 10.1029/2009gl041191

Viall, N. M., Spence, H. E., Vourlidas, A., & Howard, R. (2010). Examining Periodic Solar-Wind Density Structures Observed in the SECCHI Heliospheric Imagers. *Solar Physics*, *267*(1), 175–202. doi: 10.1007/s11207-010-9633-1

Viall, N. M., & Vourlidas, A. (2015). Periodic Density Structures and the Origin of the Slow Solar Wind. *The Astrophysical Journal*, *807*(2), 176. doi: 10.1088/0004-637x/807/2/176

Villante, U., Francia, P., Vellante, M., Giuseppe, P. D., Nubile, A., & Piersanti, M. (2007). Long-period oscillations at discrete frequencies: A comparative analysis of ground, magnetospheric, and interplanetary observations. *Journal of Geophysical Research - Space Physics*, *112*(A), A04210. doi: 10.1029/2006ja011896

Villante, U., & Tiberi, P. (2016). Occurrence and characteristics of nighttime ULF waves at low latitude: The results of a comprehensive analysis. *Journal of Geophysical Research: Space Physics*, *121*(5), 4300–4315. doi: 10.1002/2015ja022137

Ziesolleck, C. W. S., & McDiarmid, D. R. (1995). Statistical survey of auroral latitude Pc 5 spectral and polarization characteristics. *Journal of Geophysical Research: Space Physics*, *100*(A10), 19299. Retrieved from `http://adsabs.harvard.edu/cgi-bin/nph-data\_query?bibcode=1995JGR...10019299Z\&link\_type=ABSTRACT` doi: 10.1029/95ja00434

Zurbuchen, T. H., Fisk, L. A., Gloeckler, G., & Steiger, R. v. (2002). The solar wind composition throughout the solar cycle: A continuum of dynamic states. *Geophysical Research Letters*, *29*(9), 66–1-66-4. Retrieved from `http://adsabs.harvard.edu/cgi-bin/nph-data\_query?bibcode=2002GeoRL..29i..66Z\&link\_type=ABSTRACT` doi: 10.1029/2001gl013946

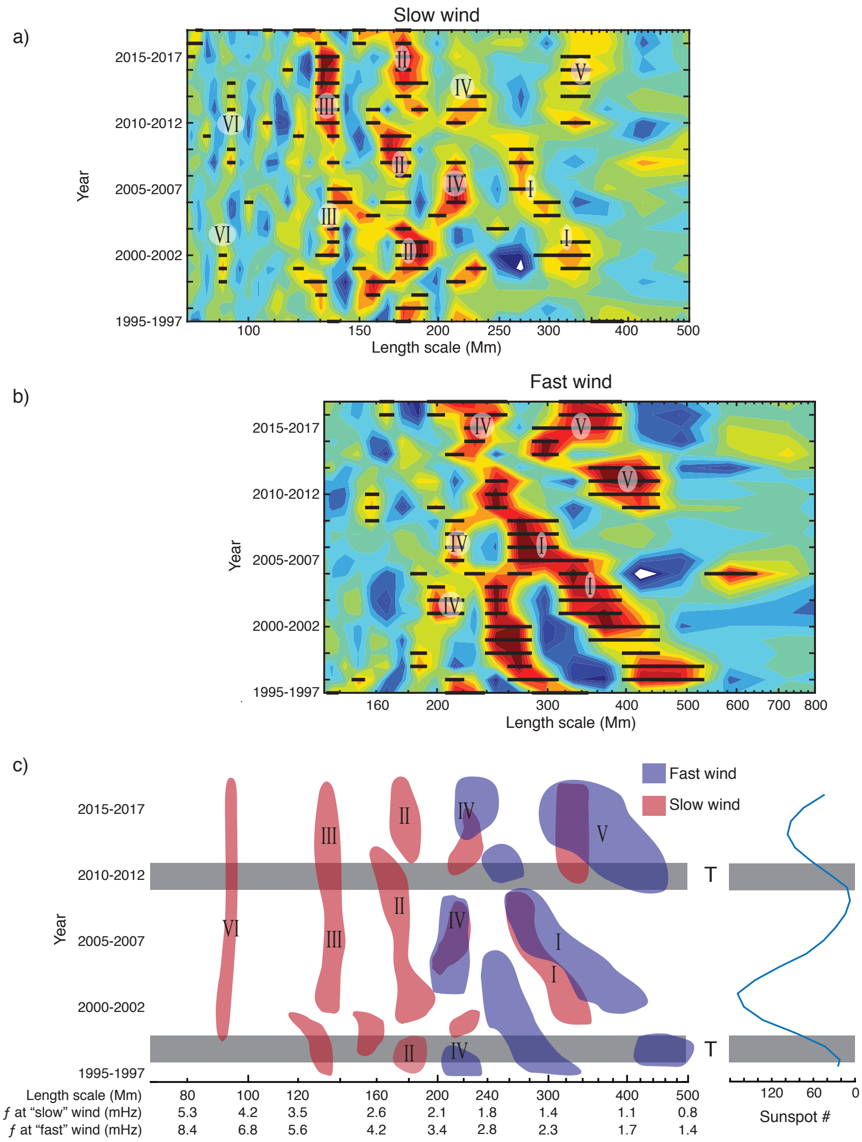

Figure 10. The contour plots (a) and (b) are the addition of the normalized (to the peak value) residuals for both the BPL and AR(1) derived occurrence distributions for the slow and fast wind. Red indicates areas of enhancement observed in both OD residuals, blue indicates areas where both found length scales significantly below the background fit, and green indicates regions near the background or areas where BPL and AR(1) were in disagreement. The bars superimposed on (a) and (b) are from Figure 8(e) and (f), and indicate length scales that exceeded the background by 2σ. The schematic (c) is a pictorial representation of (a) and (b) combined, and includes the 3-year running average of sunspot number, and locations of the terminator. slow wind is 420, fast 675 ** Need to get last 2 years of sunspot data

Figure 1.

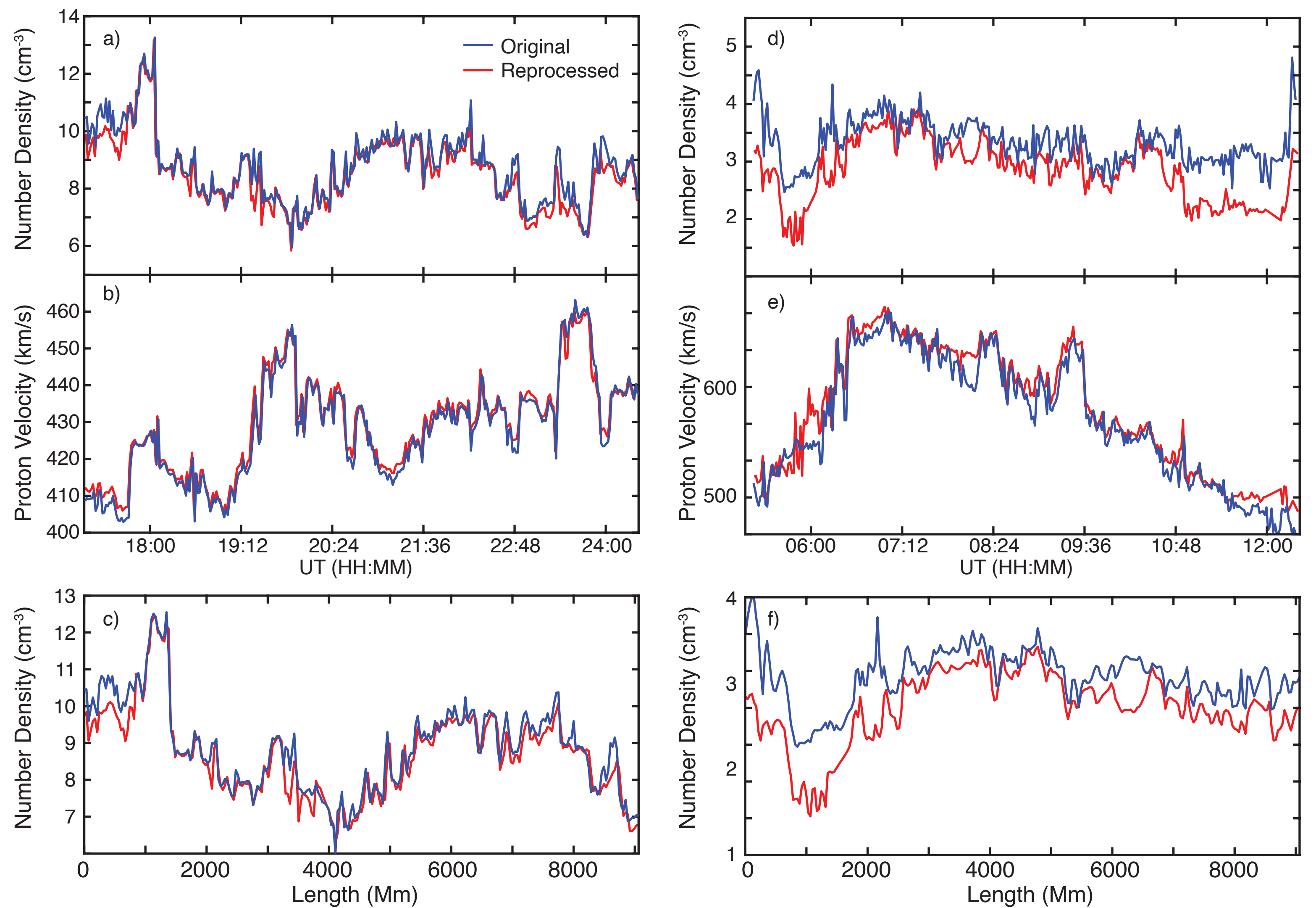

a)
b)
c)
d)
e)
f)
Original
Reprocessed
Number Density (cm^{-3})
Proton Velocity (km/s)
UT (HH:MM)
Length (Mm)
18:00
19:12
20:24
21:36
22:48
24:00
06:00
07:12
08:24
09:36
10:48
12:00

Figure 2.

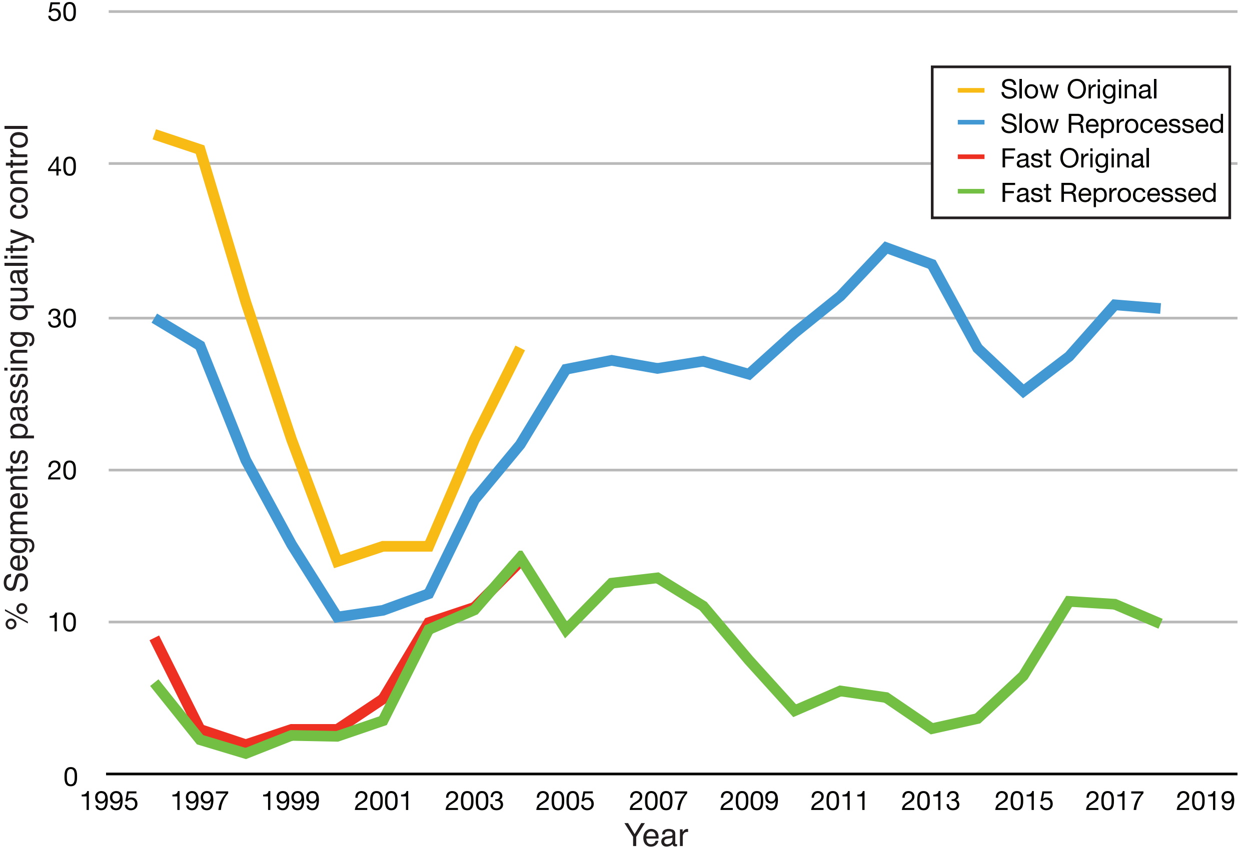

Slow Original
Slow Reprocessed
Fast Original
Fast Reprocessed
% Segments passing quality control
Year
0
10
20
30
40
50
1995
1997
1999
2001
2003
2005
2007
2009
2011
2013
2015
2017
2019

Figure 3.

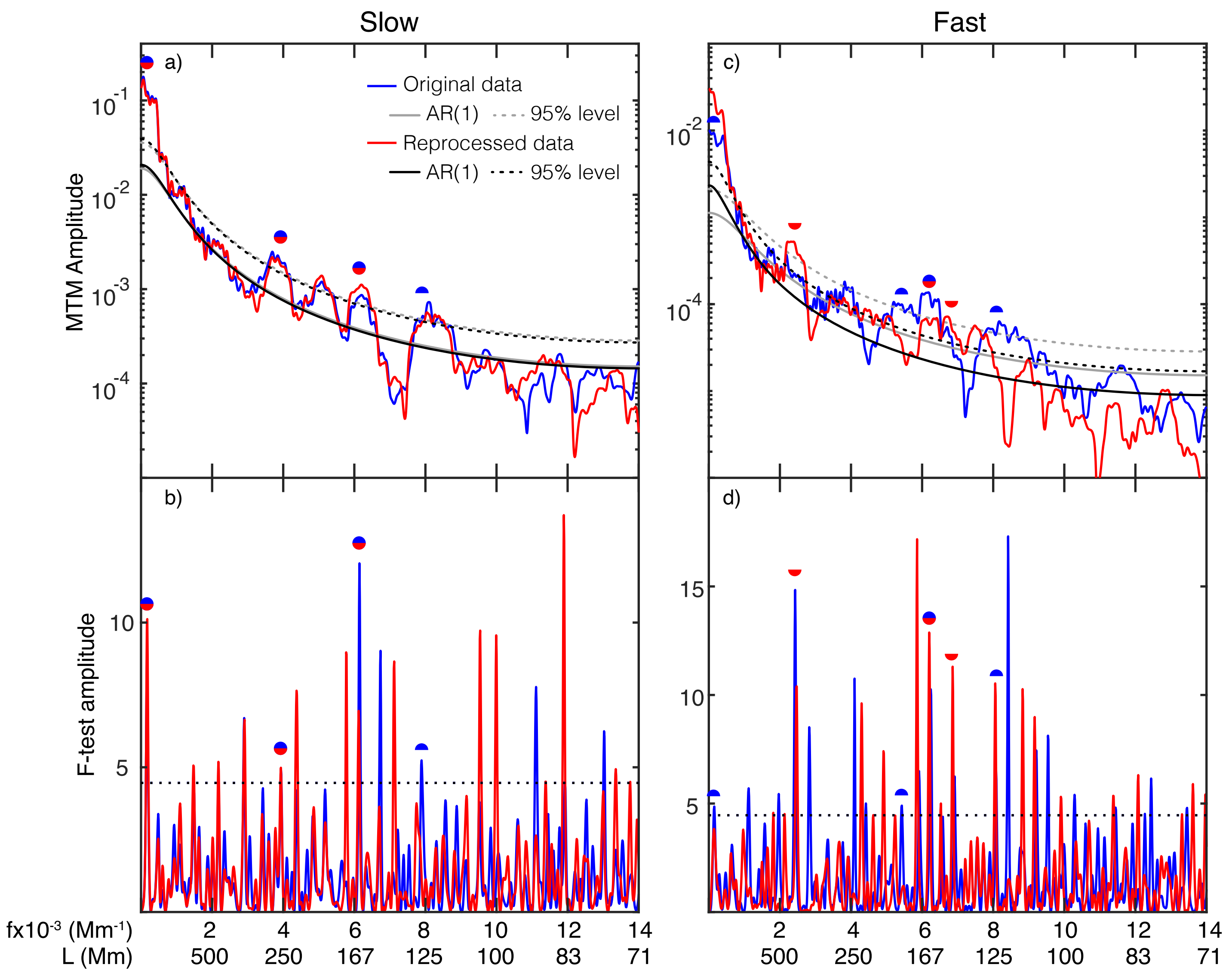

Slow
Fast
a)
b)
c)
d)
Original data
AR(1)
95% level
Reprocessed data
AR(1)
95% level
MTM Amplitude
F-test amplitude
fx10^-3 (Mm^-1)
L (Mm)
2
4
6
8
10
12
14
500
250
167
125
100
83
71

Figure 4.

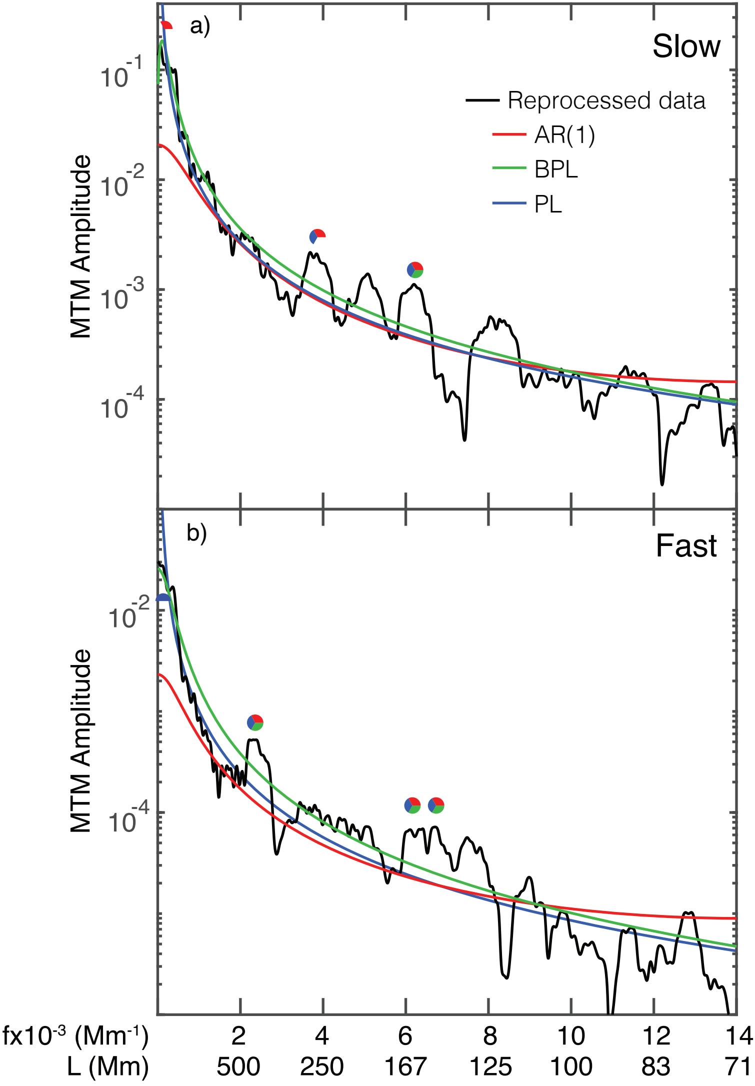

a)
Slow
Reprocessed data
AR(1)
BPL
PL
MTM Amplitude
10^{-1}
10^{-2}
10^{-3}
10^{-4}
b)
Fast
MTM Amplitude
10^{-2}
10^{-4}
fx10^{-3} (Mm^{-1})
2
4
6
8
10
12
14
L (Mm)
500
250
167
125
100
83
71

Figure 5.

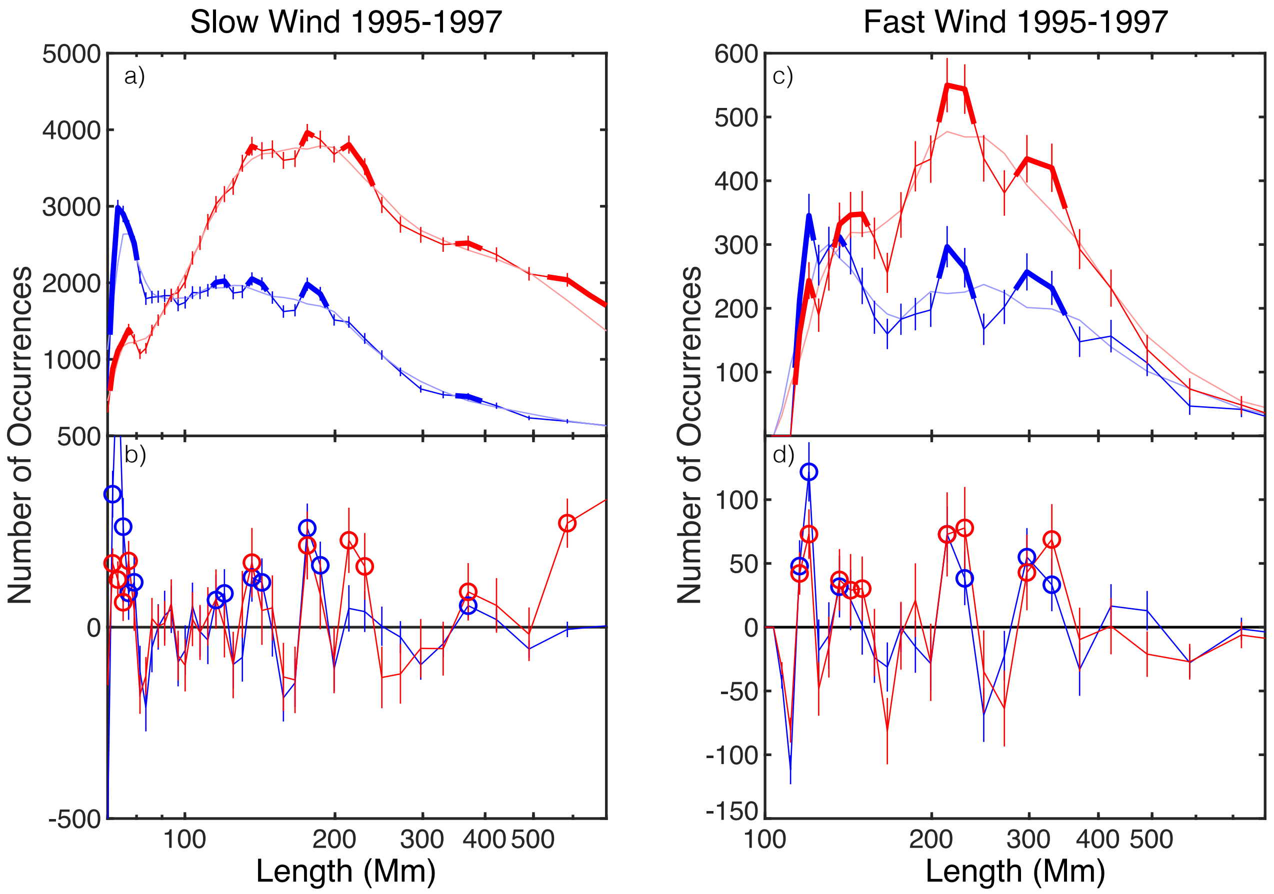

Slow Wind 1995-1997
Fast Wind 1995-1997
a)
b)
c)
d)
Number of Occurrences
Number of Occurrences
Length (Mm)
Length (Mm)
5000
4000
3000
2000
1000
500
0
-500
100
200
300
400
500
600
500
400
300
200
100
100
50
0
-50
-100
-150
100
200
300
400
500

Figure 6.

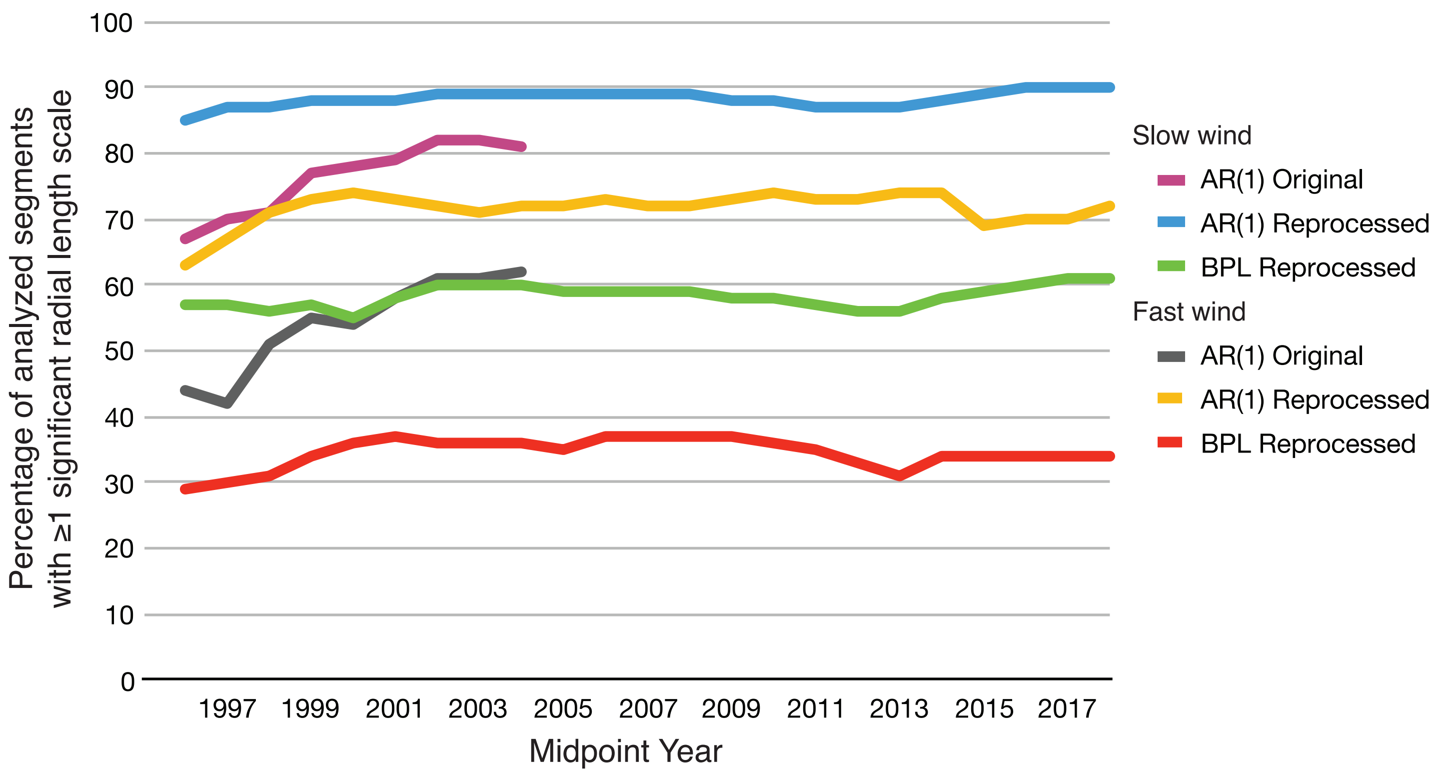

Percentage of analyzed segments with ≥1 significant radial length scale
100
90
80
70
60
50
40
30
20
10
0
1997
1999
2001
2003
2005
2007
2009
2011
2013
2015
2017
Midpoint Year
Slow wind
AR(1) Original
AR(1) Reprocessed
BPL Reprocessed
Fast wind
AR(1) Original
AR(1) Reprocessed
BPL Reprocessed

Figure 7.

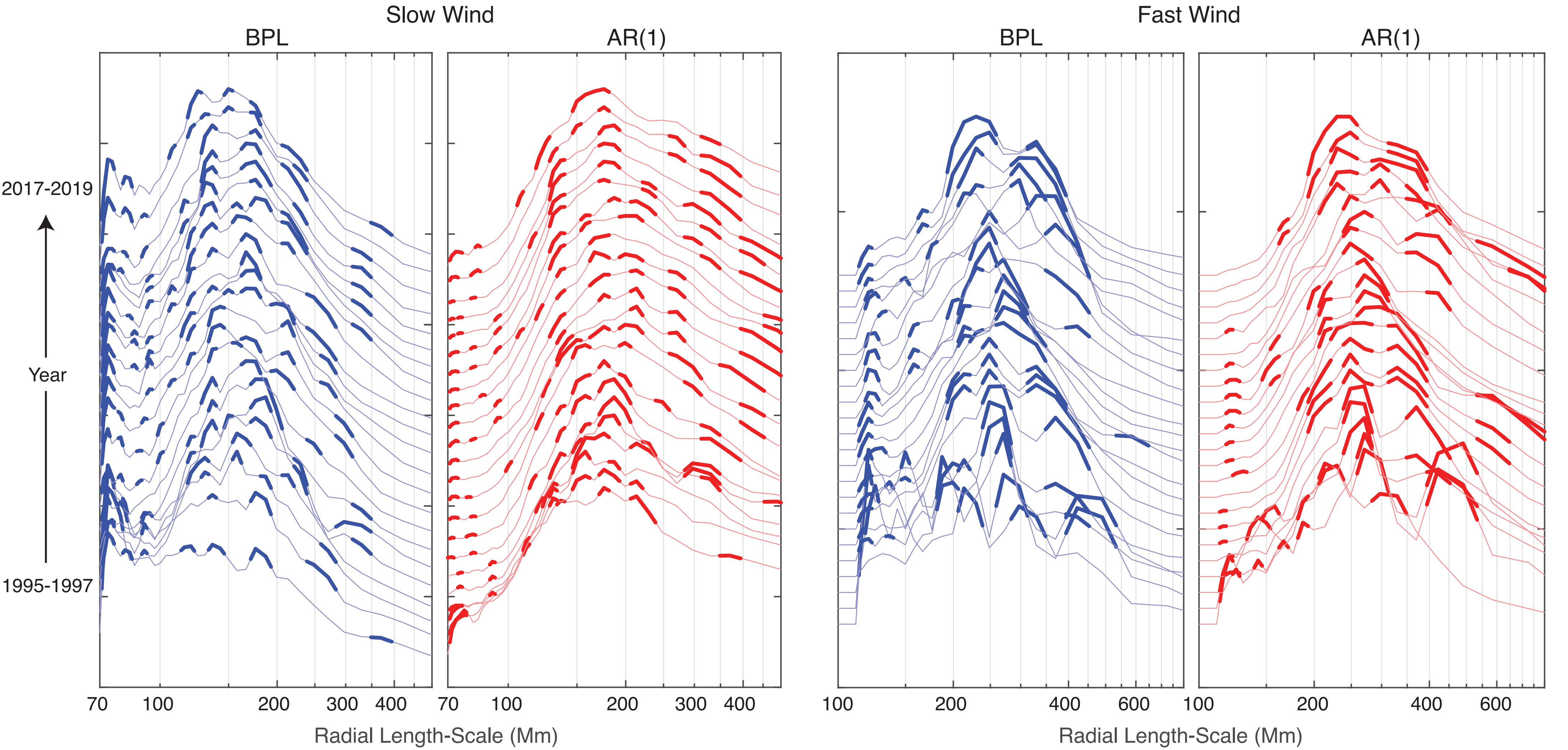

Slow Wind
BPL
AR(1)
Fast Wind
BPL
AR(1)
2017-2019
Year
1995-1997
70
100
200
300
400
70
100
200
300
400
100
200
400
600
100
200
400
600
Radial Length-Scale (Mm)
Radial Length-Scale (Mm)

Figure 8.

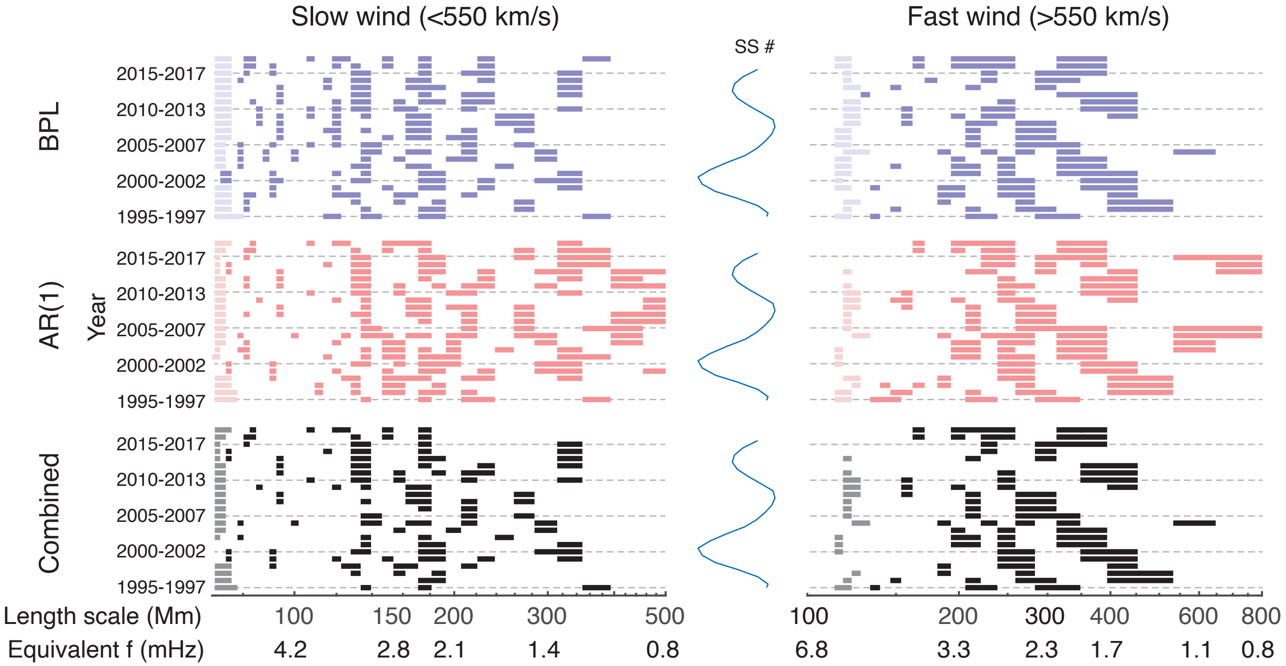

Slow wind (<550 km/s)
Fast wind (>550 km/s)
SS #
BPL
AR(1)
Combined
Year
2015-2017
2010-2013
2005-2007
2000-2002
1995-1997
Length scale (Mm)
100
150
200
300
500
100
200
300
400
600
800
Equivalent f (mHz)
4.2
2.8
2.1
1.4
0.8
6.8
3.3
2.3
1.7
1.1
0.8

Figure 9.

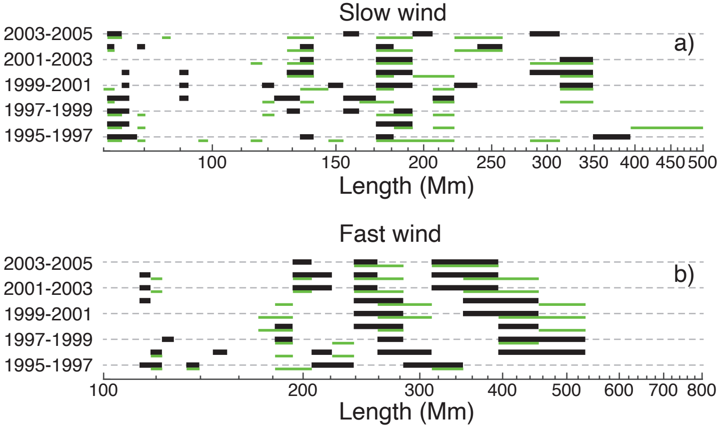

Slow wind
a)
2003-2005
2001-2003
1999-2001
1997-1999
1995-1997
100
150
200
250
300
350
400
450
500
Length (Mm)
Fast wind
b)
2003-2005
2001-2003
1999-2001
1997-1999
1995-1997
100
200
300
400
500
600
700
800
Length (Mm)

Figure 10.

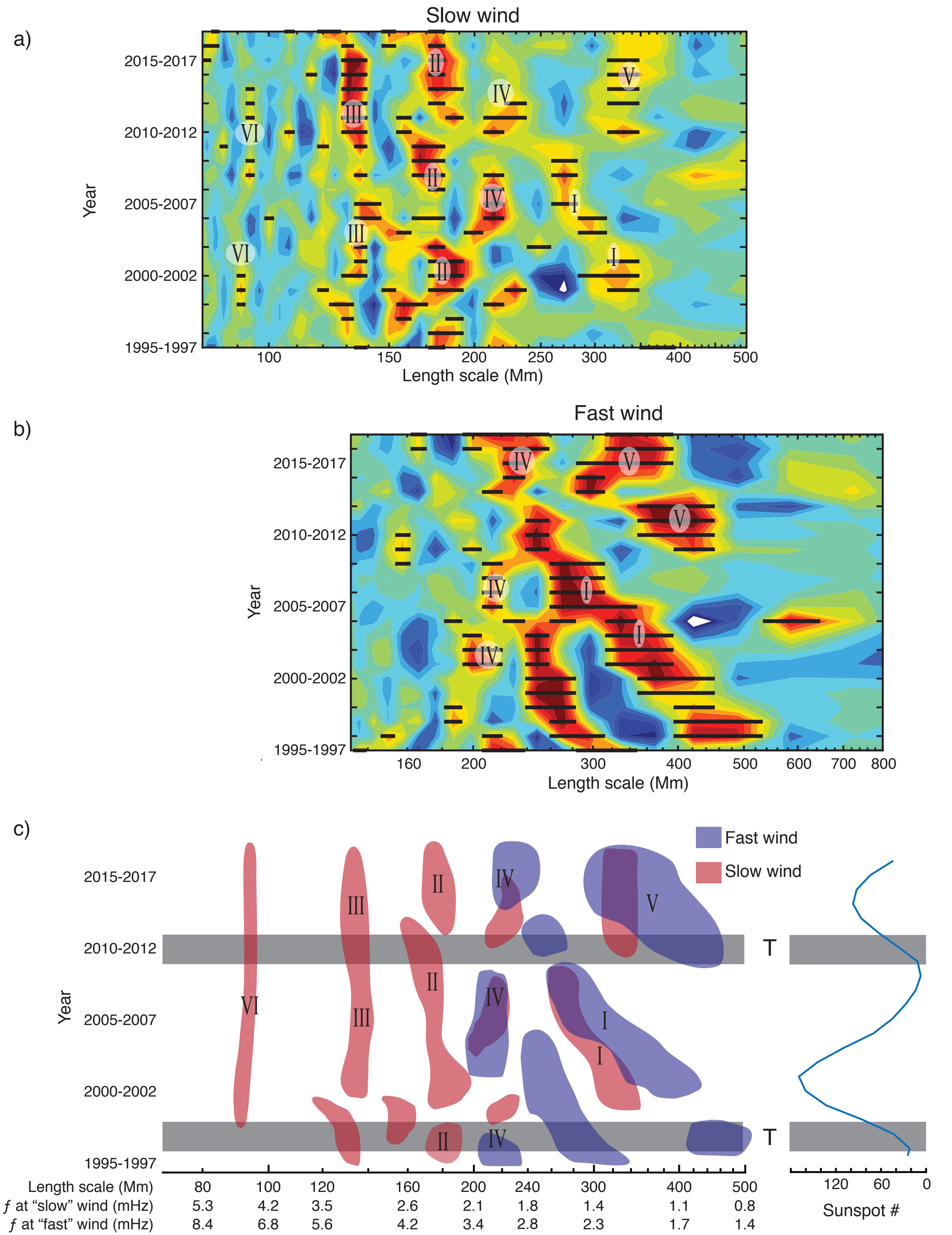
a)
Slow wind
Year
2015-2017
2010-2012
2005-2007
2000-2002
1995-1997
100
150
200
250
300
400
500
Length scale (Mm)
b)
Fast wind
Year
160
200
300
400
500
600
700
800
c)
Fast wind
Slow wind
T
Length scale (Mm)
80
120
160
240
f at "slow" wind (mHz)
5.3
4.2
3.5
2.6
2.1
1.8
1.4
1.1
0.8
f at "fast" wind (mHz)
8.4
6.8
5.6
4.2
3.4
2.8
2.3
1.7
1.4
Sunspot #
120
60
0
I
II
III
IV
V
VI